Aysun ATAKİŞİ

MULTILAYER PLASMONIC SUBSTRATES FOR SURFACE ENHANCED RAMAN SPECTROSCOPY

M.S.
2013

FATİH UNIVERSITY
The Graduate School of Sciences and Engineering

Master of Science in
Physics

MULTILAYER PLASMONIC SUBSTRATES FOR SURFACE ENHANCED RAMAN SPECTROSCOPY

by

Aysun ATAKİŞİ

July 2013

MULTILAYER PLASMONIC SUBSTRATES FOR SURFACE ENHANCED RAMAN SPECTROSCOPY

by

Aysun ATAKİŞİ

A thesis submitted to

the Graduate School of Sciences and Engineering

of

Fatih University

in partial fulfillment of the requirements for the degree of

Master of Science

in

Physics

July 2013
Istanbul, Turkey

APPROVAL PAGE

This is to certify that I have read this thesis written by Aysun ATAKİŞİ and that in my opinion it is fully adequate, in scope and quality, as a thesis for the degree of Master of Science in Physics.

_____
Assoc. Prof. Dr. Kurtuluş GÖLCÜK
Thesis Supervisor

I certify that this thesis satisfies all the requirements as a thesis for the degree of Master of Science in Physics.

_____
Prof. Dr. Mustafa KUMRU
Head of Department

Examining Committee Members

Assoc. Prof. Dr. Kurtuluş GÖLCÜK _____

Assist. Prof. Dr. Ramazan ÖZTÜRK _____

Assoc. Prof. Dr. Sadık GÜNER _____

It is approved that this thesis has been written in compliance with the formatting rules laid down by the Graduate School of Sciences and Engineering.

_____
Prof. Dr. Nurullah ARSLAN
Director

July 2013

MULTILAYER PLASMONIC SUBSTRATES FOR SURFACE ENHANCED RAMAN SPECTROSCOPY

Aysun ATAKİŞİ

M.S. Thesis – Physics
July 2013

Thesis Supervisor: Assoc. Prof. Dr. Kurtuluş GÖLCÜK

ABSTRACT

Surface enhanced Raman scattering (SERS) has received considerable attention in recent years because of its ability to detect chemical and biological analytes at very low concentrations. The Raman scattering is enormously enhanced when the analytes are adsorbed on a roughed metal surface or located nearby metal nanoparticles. Therefore, there is great interest in developing SERS active substrates. In this thesis, $Ag/SiO_2/Ag$ SERS active multilayer thin films were prepared using e-beam evaporation method on quartz support to investigate the effect of dielectric SiO_2 spacer on the enhancement factor (EF) of SERS substrates. The thickness of the SiO2 layer was varied (20nm, 40nm, 60nm and 120 nm), while keeping the Ag thickness constant at 30 nm. The prepared discontinuous metallic silver films were characterized through SEM, AFM, XRD and UV-VIS measurements. The XRD study revealed the Ag nanoparticles on the surface of the films represented face-centered cubic crystal structures. The average grain size of silver nanoparticles was found to be around 21.5 nm. The surface plasmon resonance peak positions were shifted as SiO_2 thickness varied. The SERS enhancement factors of multilayer films were investigated using Rhodamine 6G (R6G) molecule. It was found that the SiO2 layer greatly altered the Raman intensity. The SERS EF of the $Ag/SiO_2/Ag$ thin films increased 4-20 folds compared to the single Ag film. The highest enhancement factor was found to be 5.69×10^5 for the multilayer film with 120 nm SiO_2 gap. The multilayer films were also annealed at 450°C for 30 min. The thermal annealing affected the surface plasmon resonance absorptions and SERS EF values. After annealing, the SERS EF of the $Ag/SiO_2/Ag$ multilayer films increased about 25 times.

Keywords: SERS, $Ag/SiO_2/Ag$, R6G, Enhancement Factor, Surface Plasmon, E-Beam.

ÇOK KATMANLI PLAZMONİK ALTTAŞLARIN YÜZEYDE GÜÇLENDİRİLMİŞ RAMAN SPEKTROSKOPİSİ

Aysun ATAKİŞİ

Yüksek Lisans Tezi – Fizik
Temmuz 2013

Tez Danışmanı: Assoc. Prof. Dr. Kurtuluş GÖLCÜK

ÖZ

Son yıllarda Yüzeyde artırılmış Raman Saçılması (SERS) düşük konsantrasyonlarda kimyasal ve biyolojik analitlerin tespit edilmesi yeteneğine sahip olduğu için dikkate değer bir önem kazanmıştır. Analitlerin pürüzlü metal yüzeylerine absorbe olması veya metal nanoparçacıklarının yakınına yerleşmeleri sonucu Raman saçılması çok miktarda artmıştır. Bu nedenle SERS aktif alttaşlarının geliştirilmesine olan ilgi önemli ölçüde artmıştır. Bu tezde, SERS aktif alttaşlarında kullanılan dielektrik SiO_2'nin Güçlendirme Çarpanı (EF)'ne olan etkisini incelemek için elektron buhar biriktirme (EBB) tekniği kullanılarak $Ag/SiO_2/Ag$ (gümüş/silika/ gümüş) çok katmanlı SERS aktif alttaşları hazırlanmıştır. Ag katmanlarının kalınlığı 30 nm tutularak SiO_2 katmanının kalınlığı sırasıyla 20 nm, 40 nm, 60 nm ve 120 nm olarak değiştirilmiştir. Hazırlanan süreksiz metalik gümüş filmleri SEM, AFM, XRD ve UV ölçümleriyle karakterize edilmiştir. Film yüzeyindeki Ag nanoparçacıkların fcc kristal yapısında olduğu XRD çalışmasıyla ortaya çıkarılmıştır. Ag nanoparçacıklarının ortalama boyutları 21,5 nm olarak bulunmuştur. Yüzey plazmon rezonans pik konumları, değişen SiO_2 kalınlığıyla kaymıştır. Çok katmanlı ince filmlerin SERS Güçlendirme Çarpanı Rodamin 6G (R6G) molekülü kullanılarak araştırılmıştır. SiO_2 katmanının Raman şiddetini büyük ölçüde değiştirdiği belirlenmiştir. Çok katmanlı $Ag/SiO_2/Ag$ ince filmlerinin SERS Güçlendirme Çarpanı tek katmanlı Ag filmleri ile karşılaştırıldığında 4-20 kat artmıştır. Çok katmanlı filmler için Güçlendirme Çarpanı en fazla 120 nm SiO_2 kalınlığı için 5.69×10^5 bulunmuştur. Çok katmanlı filmler 450 derecede 30 dakika boyunca tavlanmıştır. Termal tavlama, yüzey plazmon rezonans absorbsiyonunu ve Güçlendirme Çarpanını etkilemiştir. Tavlama sonunda $Ag/SiO_2/Ag$ çok katmanlı filmlerin Güçlendirme Çarpanları 25 kat artmıştır.

Anahtar Kelimeler: SERS, $Ag/SiO_2/Ag$, R6G, Güçlendirme Çarpanı, Yüzey Plazmon, E-beam.

To my parents

and

To my fiancé

ACKNOWLEDGEMENT

Foremost, I would like to express my sincere appreciation to my advisor Assoc. Prof. Dr. Kurtuluş GÖLCÜK for the continuous support of my thesis study and research, for his patience, motivation, and immense knowledge.

I thank Assoc. Prof. Dr. Sadık GÜNER, for his technical guidance and assistance on the preparation of thin films. The technical assistance of Osman GÜRBÜZ is also gratefully acknowledged. I am very thankful to the head of the Physics department, Prof. Dr. Mustafa KUMRU, for his valuable suggestions and comments. I also want to thank all the members of Physics Department for providing me an excellent education and research environment. I owe many thanks, especially to my Biophotonics Research Group friends, İsmail AKYOL and Onur DURUCAN whose support has been invaluable.

I express my thanks and appreciation to my parents for their understanding, motivation and patience throughout my life. Lastly, I am thankful to all colleagues and friends who made my stay at the university a memorable and valuable experience.

TABLE OF CONTENTS

LIST OF TABLES

TABLE

LIST OF FIGURES

FIGURE

LIST OF SYMBOLS AND ABBREVIATIONS

SYMBOL/ABBREVIATION

A	Absorbance
AFM	Atomic Force Microscopy
Ag	Silver
C	Concentration
D	Particle diameter size
EF	Enhancement Factor
FDTD	Finite Difference Time Domain
I	Intensity
IR	Infrared
M	Molarity
R6G	Rhodamine-6G
SEM	Scanning Electron Microscope
SERS	Surface Enhanced Raman Spectroscopy
SiO_2	Silica
SPR	Surface Plasmon Resonance
T	Transmittance
UDEDM	Uniform deformation energy density model
UDM	Uniform deformation model
USDM	Uniform deformation stress model
XRD	X-ray Diffraction
Y	Modulus of elasticity
δ	Dislocation energy
ε	Absorptivity
ℓ	Path length
σ	Stress

CHAPTER 1

INTRODUCTION

Surface enhanced Raman scattering (SERS) is a powerful surface-sensitive technique that enhances Raman scattering by molecules adsorbed on rough metal surfaces or by nearby plasmonic nanostructures. The enhanced Raman signals allow detection of analytes at very low concentration down to single molecules [1-3]. Surface Enhanced Raman Scattering (SERS) was revealed first approximately thirty years ago. Both theoretical and experimental studies have tried to understand the SERS mechanisms. Its application has steadily increased in physics, chemistry and biosciences. SERS transformed the conventional Raman spectroscopy into a high-sensitive analytical device by increasing the intensity of vibration signals of molecule as 10^3-10^{14} times [1-5].

The enhancement of Raman Scattering is represented by two mechanisms; electromagnetic and chemical mechanisms [5-8]. First, the electromagnetic theory is related to signal enhancement that is provided by plasmon resonances in the metal substrates. Plasmon resonances are occurred when the electromagnetic radiation interacts with metal substrates. This theory is observed on the local surface plasmon resonance of metallic nanostructures. Second, the chemical theory, there is a charge transition between absorbed species and the metal surface. When the molecule is in contact with the surface, the charge transition starts. So, the cross section of absorbed molecules is increased. Thus, the chemical enhancement is observed [7-12]. Preparation of SERS-active surface which is about the enhancement of the Raman scattering on the metallic surfaces has become increasingly important in different research areas for SERS applications. For this purpose, the SERS-active surfaces or substrates which have different morphological features are developed by using the lithography, chemical etching, chemical vapor deposition, and electron radiation methods [4-9].

The SERS-active substrates are also obtained by spreading the colloidal metal nanoparticles on surfaces or by mixing analyte which will be investigated [10].The molecules absorbed on metallic surface are useful for SERS measurements when they have large cross-section under certain conditions. The intensity of Raman scattering or Raman enhancement directly depends on chemical nature of molecules that are absorbed on metal surface, the type of used metal surface and metal structure. Generally, metals such as Au, Ag and Cu provide the activity of SERS. The rough surfaces made of this metal or colloidal nanoparticles cause the SERS effect [1]. In the applications of obtained SERS active substrates, "sensitivity" and "reproducibility" emerge as the two important parameters [1-3]. Up to now, different methods have been developed to produce a cost-effective and high amount of substrate using in the SERS applications [4-6]. In these methods, hot spots which are related to enhance the electric field around the metal are tried to be obtained. For example, Ag-coated silicon nanotubes [8], Ag or Au nanoparticles embedded in the polycarbonate [9], the membranes were made. Sensitivity and reproducibility of these substrates or colloidal nanoparticles are less because of having low amount of hot spots and clustering.

SERS has important applications in many areas of chemistry, like chemical analysis, [14, 15] catalysis [15, 16] and biological systems [17-20] to characterize proteins, enzymes at interfaces. SERS can be used to determine functional groups of the adsorbed species that are responsible for the interaction with the surface and the compatibility of adsorbed molecule on the surface [21].

The roughened metallic electrodes are also used as SERS active substrates [10-13]. But they have lower SERS EF than metallic nanoparticles. Kyoung *et al* suggested that considering the SPR interaction in bimetallic systems and using dielectric gap between metallic multilayer systems remarkably changed the SERS EF [13]. For the periodic metallic structure allow reproducibility and long-term stability while the dielectric interlayer can enhance the sensitivity [13]. The enhancement factor of $Ag/SiO_2/Au$ multi-segment layer was found as approximately 10^6. The Qiao Min and coworkers produced the $Ag/TiO_2/Au$ multilayer films. According to this study, the effect of insulator layer thickness variation that was 40 nm and 200 nm changed the peak enhancement 45.4 and 51.6 times respectively [23]. So the enhancement factor was increased while the insulating layer thickness was increased.

There is also an increasing research interest in literature in metal-insulator-metal film structures recently because of their plasmonic features and high signal enhancement properties. They can serve as models sub-wavelength waveguides, for understanding the plasmon resonance frequencies arising from LSPR–surface plasmon polariton (SPP) interactions, and as a robust and easy to fabricate SERS substrates with high signal amplification [13].

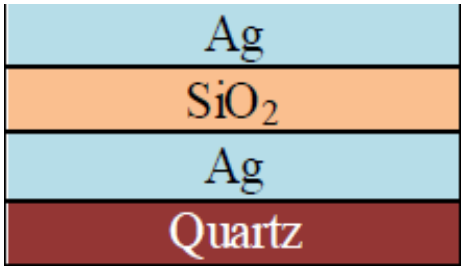

Figure 1.1 Schematic of the Ag/SiO_2/Ag multilayer SERS substrate on Quartz substrate.

The aim of this thesis is to prepare and investigate the plasmonic effects of multilayer films in the form of Ag / SiO_2 / Ag with different SiO_2 thickness. In this thesis, Metal/Insulator/Metal (M/I/M) thin films as shown in Fig. 1.1 were produced by E-Beam evaporation technique. The thickness of insulator layer SiO_2 was varied as 20 nm, 40 nm, 60 nm and 120 nm. The thickness of the metal (Ag) layers was kept constant at 30 nm. The produced thin films were characterized by using characterization techniques such as Raman Spectroscopy, Atomic Force Microscopy, Scanning Electron Microscopy, X-Ray Diffractometer and UV-Vis Spectroscopy. These characterization techniques were explained in Chapter 2. The results of the characterization methods were given in detail in Chapter 3. The surface enhancement of Raman scattering (SERS) effects were investigated for the Ag single layer and Ag/SiO_2/Ag multilayer plasmonic thin films and their results were discussed comparatively in Chapter 3.

CHAPTER 2

MATERIALS AND METHODS

2.1 MATERIALS

Rhodamine 6G dye was purchased from Sigma Aldrich to determine the SERS enhancement factor of the Ag/SiO_2/Ag films. Ag (99.9 % purity) and SiO_2 targets were purchased from Kurt J. Lesker Company to produce multilayer thin films. All the products were used as their received.

2.2 E-BEAM EVAPORATION TECHNIQUE

E-Beam evaporation technique is a type of physical vapor deposition (PVD) technique. The aim of this technique is the using the phase change of a material from the condensed to the vapor phase. The E-Beam evaporation technique is mainly related to both dielectric and metal depositions. A common variety of materials that can be evaporated consist of refractor metals (tungsten, etc.), low vapor pressure metals (platinum, etc.) and alloys [24].

The schematic of evaporation system is shown in Fig. 2.1 [25]. The magnetic field is applied perpendicular to the propagation direction of the electron beam and the magnetic field is used to bend and shape the electron beam. This is a precaution to protect the source of e-beam from the vapors during the evaporation process. The evaporation process is started in vacuum under the 10^{-5} mbar or less than this pressure. Since, the high vacuum is needed to keep up with a large mean free path of evaporant

material. According to e-beam evaporation technique, the electron beam gun has the filament inside must be sufficiently heated to emit electron. Electron emission occurs from a hot filament cathode made up of tungsten.

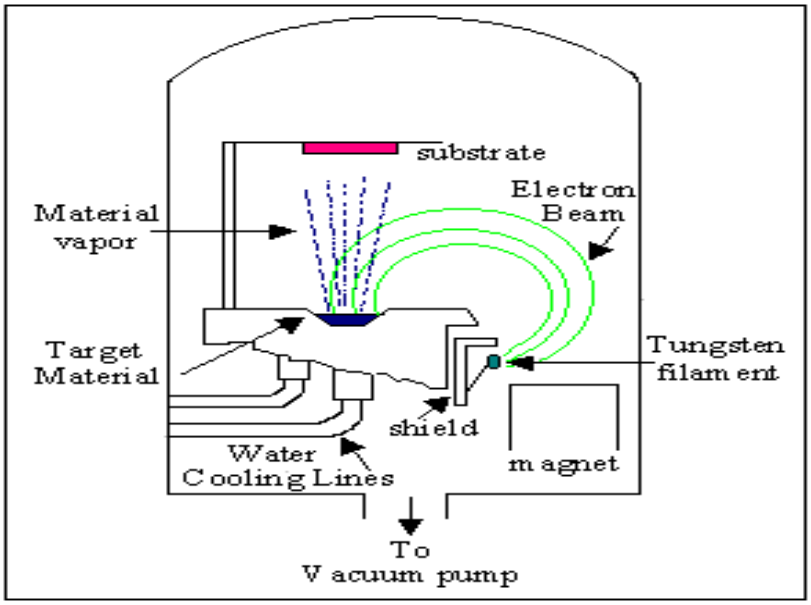

Figure 2.1 Schematic diagram of E-Beam Evaporation system.

The electron beam which is deflected and accelerated by the electric field and magnetic field is focused on the target material so as to evaporate it. When the electron beam hits the target surface, the kinetic energy of motion is converted into thermal energy. The emitted energy by a single electron is quite small and the heating is performed simply through the numerous numbers of electrons which are stroked to the evaporant surface. This energy is the energy which evaporates the target material. The material heats with time and causes clusters of material atoms to sublime [24]. Effectively, the material becomes hotter than the focused electron beam. Because the intensity of heat is formed by electron beam, being a crucible made of carbon has high melting temperature, the evaporant holder has to be water cooled to prevent it from the damage of melting. The deflection apparatus are designed by using permanent magnets or electromagnets to form a field which is related to shape and path of the electrons. This is required for the electrons which are emitted in a random manner and must be all

directed to the very small area where the evaporation is occurred. A magnetic field is used, since it can attract or repel the negatively charged electrons directly. The material can cover to the surfaces of the chamber included region with the sample. Typically, the sample can be protected by a shutter. When the stable deposition rate is established, the deposited sample is related to flux of atoms which can hit to target surface with respect to time which is related to deposition rate. Therefore the amount of deposited material can be estimated correctly [24].

In this thesis, Mantis E-beam evaporations system was used. The system includes two single pocket high energy (6 kW maximum powers) electron beam evaporators and a RF ion source for dry etching purposes. Base chamber was pumped by a turbo molecular pump until 10^{-8} Torr vacuum level reached. The thickness of the films was monitored with QCM.

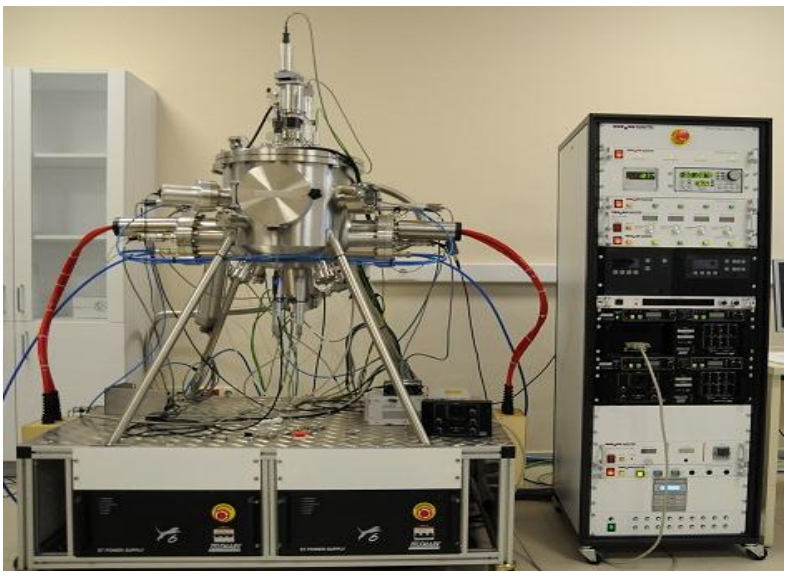

Figure 2.2 Mantis E-Beam Evaporation systems.

2.3 AFM (ATOMIC FORCE MICROSCOPY)

Atomic Force Microscope (AFM) is an important technique for imaging surface morphology. AFM devices operate in two different modes in general. In static (contact) mode, the needle tip is fixed at a certain height. However, the downward force applied

to the tip of the needle may damage the sample surface when the applied force is more than necessary. In the dynamic (non-contact) mode which is applied to prevent the surface to damage; the needle tip is contacted and removed in very short periods with oscillation movement. In this mode that is also known as vibration mode, the oscillation amplitude of needle tip changes with respect to forces between tip and sample. The tapping mode AFM images of the films were acquired using a Park AFM (XE-100, Park AFM, Korea), supported on a Minus-K (25BM-6, Minus-K, Inglewood, CA) vibration isolation base.

2.4 XRD (X-RAY DIFFRACTION)

X-Ray Powder Diffraction (XRD) technique is an analytical technique that is used to get information about the crystalline material especially its phase identification and the dimension of its unit cells. X-ray powder diffraction is most widely used for the identification of crystalline structure of materials.

Mainly, X-ray diffraction is based on constructive interference of monochromatic X-rays and a crystalline sample. X-rays which are formed by a cathode ray tube is filtered to get a monochromatic radiation and parallelized to concentrate and fell directly upon the sample. The interaction between the incident rays and the sample occur constructive interference and a diffracted ray. If the conditions satisfy for Bragg's Law ($n\lambda=2d\sin\theta$) which is related to diffraction angle and the lattice spacing in a crystalline sample. Then, the diffracted X-rays are detected, processed and counted. With scanning the sample among a range of 2θ angles, all diffraction directions of the lattice should be obtained through the random orientation of the material which is powered. A key component of all diffraction is the angle (θ) between the incident and diffracted rays.

X-ray diffraction pattern of the samples were recorded using a Rigaku Smart Lab SEA 107 X-Ray diffractometer shown in Fig. 2.3 with Copper K_α (λ=1.54056 A°) radiation.

Figure 2.3 X-ray Diffraction systems.

2.5 UV-VIS SPECTROSCOPY

UV-Vis spectroscopy is a study about how a sample responds to light. When a light beam passes through a substance or a solution, some of the light beam may be absorbed and the transmitted by the sample [26-29]. The ratio of the intensity of the light which is entered the sample (I_0) to that exciting the sample (I_t) at a particular wavelength is defined as the transmittance (T). This is usually represented as the percentage transmittance (%T) which is multiply by 100.

$$\%T = \left(\frac{I_0}{I_t}\right) x100 \tag{2.1}$$

The absorbance (A) of a sample is calculated by taking the negative logarithm of the transmittance Eq. (2.1).

$$A = -\log(T) \tag{2.2}$$

A surface plasmon (SP) is an electro-magnetic wave propagating along the surface of a thin metal layer. When the metals are stimulated by incident light, the collective oscillation of electrons in a metal is called as surface plasmon resonance (SPR). When the frequency of light photons is appropriate the natural

frequency of surface electrons which are oscillated against the restoring force of positive nuclei [30]. These oscillations are very sensitive to any change of this boundary, such as the adsorption of molecules to the metal surface. The surface plasmon resonance curves of the $Ag/SiO_2/Ag$ films were determined using a UV-VIS spectrometer in transmission mode. UV-VIS spectra of thin films were recorded using Thermo Scientific EVO 300 spectrophotometer. The measurements were taken between 300 nm and 1100 nm.

2.6 RAMAN SPECTROSCOPY

In 1928, Indian physicist C.V. Raman found that a large part of wavelength of scattered light which is interacted with molecules has same wavelength of incident light, a very small part of wavelength of the scattered light shifts different wavelengths and this shift depends on chemical structure of molecules caused by scattering [31]. In 1931 this study was earned the Nobel Prize to him. The shift of light in different wavelengths is called Raman scattering and the physical basis of Raman scattering is inelastic scattering which occurs the result of collision between particles that make up the beam of light and molecules in the environment. Inelastic scattering is a change of the photon energy due to photon wavelength the result of collision between photon and molecules. During the scattering of light, if the energy of scattered light and energy of light which interacts with molecules are equal each other, this scattering is elastic scattering and known as Rayleigh scattering. In Rayleigh scattering, more than 10^4-10^5 times intense light occurs from than Raman scattering. For the total energy is preserved during the Raman scattering, the energy that photon gains or losses must be equal to energy that is among vibration energy levels of molecules [32]. By the determining the amount of gained or lost energy of photon, information about the vibration energy levels of molecules can be obtained and this type of spectroscopy is called as Raman Spectroscopy.

Raman spectroscopy is a type of vibration spectroscopy like IR (infrared) spectroscopy. When a sample is irradiated through the monochromatic laser source which has $h\upsilon_0$ energy in visible region or near-infrared region, a part of energy of photon is transferred to the molecules or energy of molecules are transferred to a little

number of photon. As a result of this transfer, the energy of molecule can take any value among the infinite values which are called virtual states located between the ground state and first excited state. As shown in Fig. 2.4 [33] the emitted radiation which is from excited virtual state of molecule may be three types [34]. First, as mentioned earlier Rayleigh scattering that has the same energy as excitation energy and there is no energy lost for Rayleigh scattering. Therefore the collisions between the photon and the molecule is said to be elastic. The other two types are actually type of Raman scattering as called Stokes scattering and Anti-Stokes scattering. The energy changes in the Stokes and Anti-Stokes scattering is equal to ΔE which is the difference between vibration energy levels. For the Stokes scattering, the energy of emitted light is smaller than excitation energy. For Anti-Stokes scattering, this energy is bigger than the excitation energy. According to, Boltzmann Distribution Law the number of molecules which is in the excited states before the interaction with a photon is much less than the number of molecules which is in the ground state levels. So, the probability of occurrence of Anti-Stokes scattering is less than Stokes scattering. Furthermore, the Rayleigh scattering has bigger probability of occurrence than the Raman scatters. Because, the transfer of energy to molecules to the ground state and return of molecules to the ground state are most likely event.

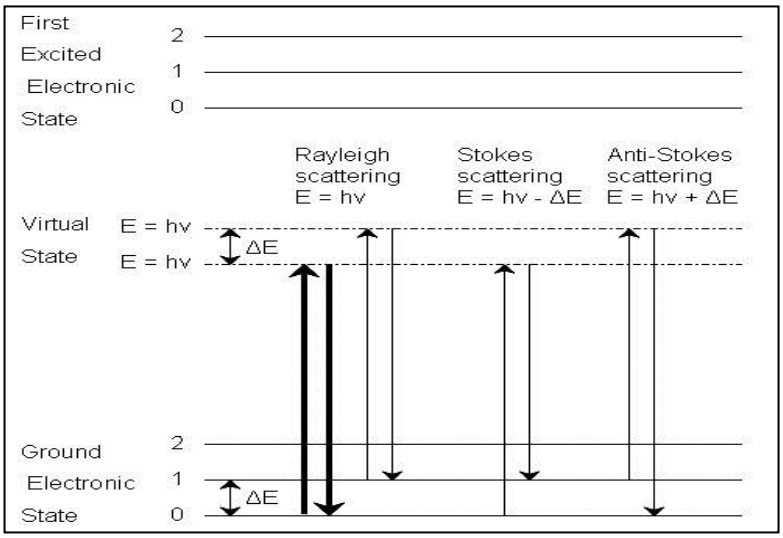

Figure 2.4 Molecular energy diagrams of Rayleigh and Raman scattering.

2.7 SERS (SURFACE ENHANCED RAMAN SPECTROSCOPY)

Surface Enhanced Raman Spectroscopy is a surface-sensitive the vibrational spectroscopy that measures the scattering process of the inelastic light. SERS is a more precise method than traditional Raman method, since it allows the determination of low concentrations of substances. SERS was first observed in 1974 by Martin Fleischman et al. [35]. Basically, it is an event that is enhanced Raman scattering by the absorbed molecules on the rough metal surfaces.

Generally, the metals such as gold (Au), silver (Ag) and copper (Cu) that are ending with d10 electron arrangement of their basic level is used in event of SERS on account of behavior of the free electron in their last orbits. The surface roughness is required for SERS and usually can be achieved by ways of electrochemical lithography or chemical etching. Furthermore, colloidal gold or silver nanoparticles in glass, mica and so on are widely used in the recent years in terms of ease of preparation. Raman scattering is enhanced as a result of the adsorbed molecules on the metal nanoparticle surface when the getting closer to the metal surface.

Theoretical and experimental studies have revealed that the intensity of SERS is directly proportional to amount of nanoparticles [35-40]. Raman scattering mainly associated with polarizability of molecule. However, SERS related with both intensity of electric field and strengthening of polarizability.

A mechanism of SERS which mechanism influences to enhancement of the Raman spectroscopy of a molecule that is adsorbed near the metal surfaces is not known completely. This topic has been discussed in a great deal of theoretical and experimental works lately. SERS effect, with increasing Raman scattering is generally caused by two different mechanisms:

(a) Electromagnetic Enhancement; in which the enhancement is caused by the surface plasmon resonance generated on the roughened metal surface,
(b) Chemical Enhancement; which involves changes to the adsorbate electronic states due to chemisorptions of the analyte.

These increases occur between molecules and metal structures. Where the enhancement factor (EF) can be up to 10^{10} -10^{12} [41], this shows that SERS is ultra-sensitive technique and can be sensed even in a molecule [42].

2.7.1 Electromagnetic Enhancement Mechanism

The Raman intensity of a molecule is directly proportional to magnitude of incident electromagnetic field. So, both the oscillation frequency of electrons which provides the conductivity in nano-structure of metals and reduced light on the metal is achieved resonances. These consisting of surface plasmons are electromagnetic waves. Fig. 2.5 [43] shows the plasmon oscillation of small metallic spheres. Coherent oscillation due to the light scattering ends to the transmission electron of small spherical metallic nanoparticles. The oscillation of electron cloud causes by the Coulomb's attraction force the between electrons and nuclei [44].

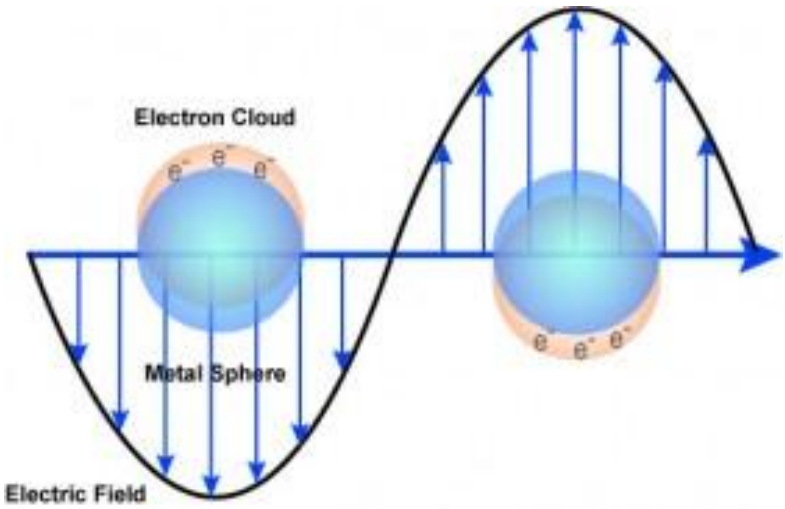

Figure 2.5 Plasmon oscillations for small metallic sphere.

Possible increase in the local electric field is calculated from sum of contribution of all dipoles which are located in the particle and electromagnetic field. This leads to stronger enhancement of Raman scattering on metal surface or molecule which is located very close to surface. The surface plasmon of particles which is very close to together coincide each other and this leads to a very severe enhancement in the Raman

scattering. Therefore, the Raman scattering enhanced and this enhancement may be approximately 10^{14}. This kind of nanometric regions is called "hot spots" [45]. Settled between these hot spots, the Raman scattering of molecules are intense.

The enhancement factor is directly depended on the gap and shape of nanoparticles on the surface. When the gap reduces electric field increases as it shown in Fig. 2.6 [46]. The electric field intensity ($|E/Eo|^2$) goes from 2 orders to 4 orders of magnitude driving Raman enhancement factors ($|E/Eo|^4$) from 4 orders to 8 orders.

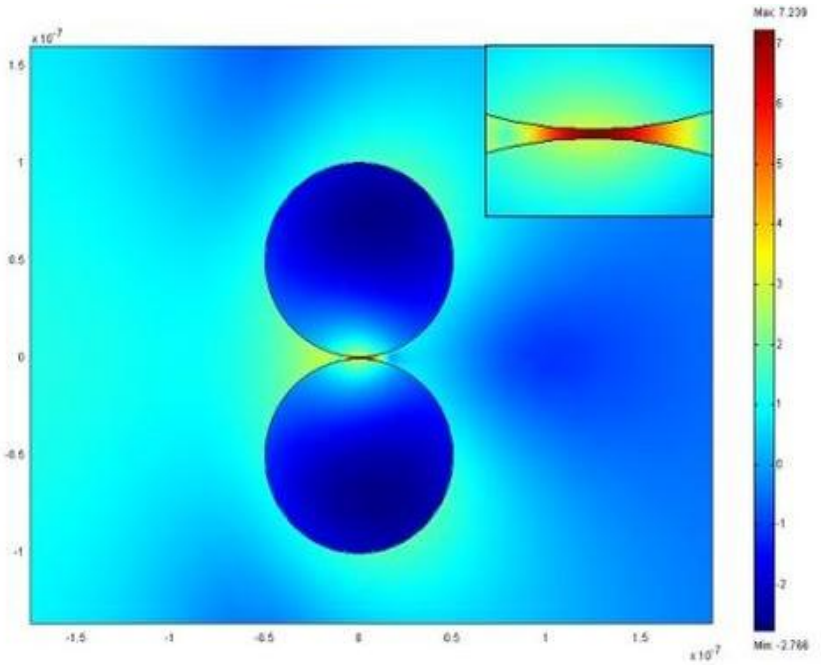

Figure 2.6 Shape and distance dependency of EM enhancement.

2.7.2 Chemical Enhancement Mechanism

Chemical enhancement is the other mechanism of SERS effect. Basically, this mechanism is related to enhance the Raman polarizability of molecule absorbed on metal surface [47]. For instance, although CO and N_2 have the same cross-section, the Raman intensity of molecules can be different from each other 200 times [48]. When a photon influences on a metal, electron in metal reacts. The electrons of molecules adsorbed on the metal surface move into the interiors of molecule and the negatively

charged excited molecule occurs. The geometry of this molecule is different than the geometry of neutral molecule. Even if the excited electron move to the metal, the molecule remains at new excited vibration energy level and makes the Raman scattering [49]. Thus, the SERS effect differences between CO and N_2 can be explained by different adsorption levels of CO and N_2 on the surface [33]. For Co is adsorbed on the silver surface better than the N_2, the charge transfer changes between metal and adsorbate. Therefore, the dependence of chemical enhancement on SERS is observed [50] and the enhancement may be only about 10^2 times.

For providing enhancement at Raman scattering, SERS active metal electrodes, SERS active metal nanoparticle colloids and metallic nano-structures developed based on SERS active substrates are used. SERS active substrates are used to biosensors, diagnostic purposes, and for the purpose of determination of low concentrations of substances.

Today, the studies with respect to surface enhancement are increasing not only the basic sciences as physics and chemistry but also applied field as bioengineering. In general, SERS is used widely in chemical bonding, genomics, proteomics, protein interactions, solid-phase synthesis studies with DNA, protein analysis, and the study of intracellular events and cancer studies. SERS leads to develop new, rapid, inexpensive methods [35-42]. Also, it provides bacterial assays in food and biomedical fields, enzyme assays, pathogen detection and even detection of bioanalyte in a range of single-molecule by using its high-sensitive property.

The Raman and SERS studies were performed using DXR Raman system. The SERS and Raman spectra of Rhodamine 6G molecules were recorded in the range 500-3500 cm^{-1} at room temperature. A 50X/0.75NA objective was used to collect back scattered photons from the samples. The laser wavelength is 532 nm and the laser power is set to 4mW. The spectra were collected in 3s.

CHAPTER 3

EXPERIMENTAL RESULTS AND DISCUSSION

3.1 PREPARATION OF $Ag/SiO_2/Ag$ THIN FILMS

Electron beam (E-Beam Evaporation) deposition technique was applied to deposit $Ag/SiO_2/Ag$ films on quartz substrates that have 1 cm^2 area and 1 mm thickness. The E-beam deposition was performed on a custom design deposition system by Mantis Deposition LTD. The SiO_2 substrates were cleaned with isopropanol and ethanol mixture in an ultra-sonic cleaner for 10 minutes.

The base chamber was evacuated, using a roughing and a turbo molecular pump, to a pressure of $3x10^{-7}$ mbar. The pressure during the deposition process was about $5x10^{-6}$ mbar. The substrates were not heated. However, a thermo-couple (K-type Chromel-Alumel) placed in contact with the substrate was used to monitor the substrate temperature. The temperature was raised from room temperature to maximum 35 °C.

We measured the deposition rate and thickness of the films with quartz crystal monitor (QCM). The Ag seed and capping layers were deposited at a constant rate of 0.40 Å/s while SiO_2 layer at a range from 0.20 to 0.45 Å/s with respect to increasing thickness. The thickness of each layer was also justified by a NanoMap 500LS profilometer. The substrates were rotated at a frequency of 12 rev/min have better uniformity. So in our work, a 30 nm Ag was deposited on the both sided SiO_2 substrate to form the initial SiO_2 substrate surface. Next, 20 nm SiO_2 layer was deposited as an interlayer. Finally, an Ag layer 30 nm was deposited on the SiO_2/Ag/glass substrate. Namely, Ag thicknesses are constant at 30 nm. SiO_2 thickness was changed as 20 nm 40 nm, 60 nm and 120 nm.

3.2 SURFACE CHARACTERIZATION OF THIN FILMS

3.2.1 SEM Measurements

The SEM images of Ag nanoparticles on the surface of $Ag/SiO_2/Ag$ multilayer plasmonic thin films were shown in Fig. 3.1. The cross sectional view of multilayer film was given in Fig. 3.2. The $Ag/SiO_2/Ag$ multilayer plasmonic thin films were annealed at 450 ^{0}C during the 30 minutes in order to examine the effect of temperature on particle size. The SEM images of $Ag/SiO_2/Ag$ multilayer thin films that have 60 nm SiO_2 thicknesses at 20 ^{0}C and 450^{0}C and $Ag/SiO_2/Ag$ multilayer thin films at 450 ^{0}C for SiO_2 thicknesses as 20 nm and 40 nm were shown in Fig. 3.3 and Fig. 3.4. As it was seen from the SEM images, the particle size of Ag nanoparticles was not uniform and the films were discontinuous. After annealing, the Ag nanoparticles seemed as slightly separated because of the thermal effect.

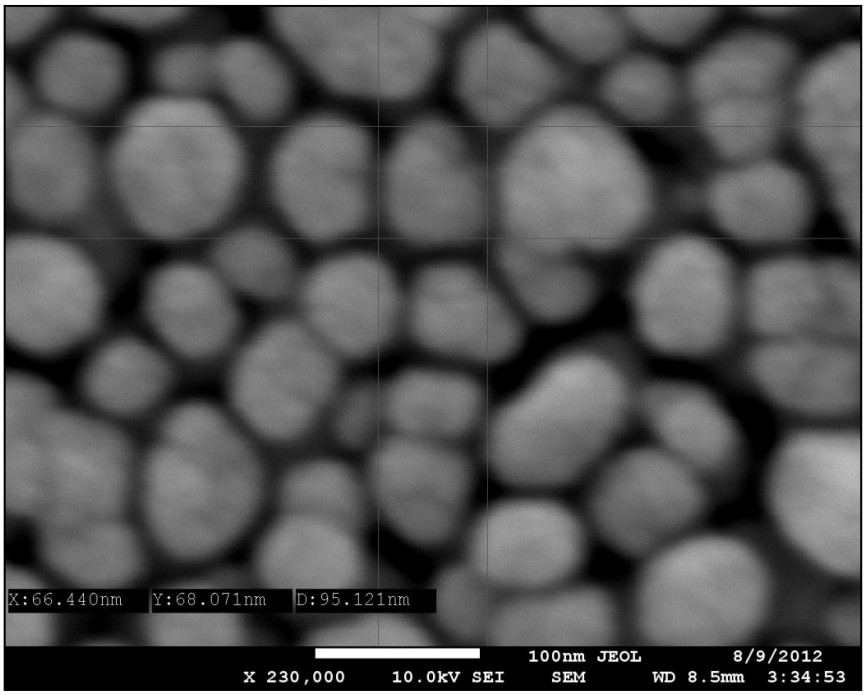

Figure 3.1 The SEM image of surface of the multilayer film. Non-uniform Ag nanoparticles are visible.

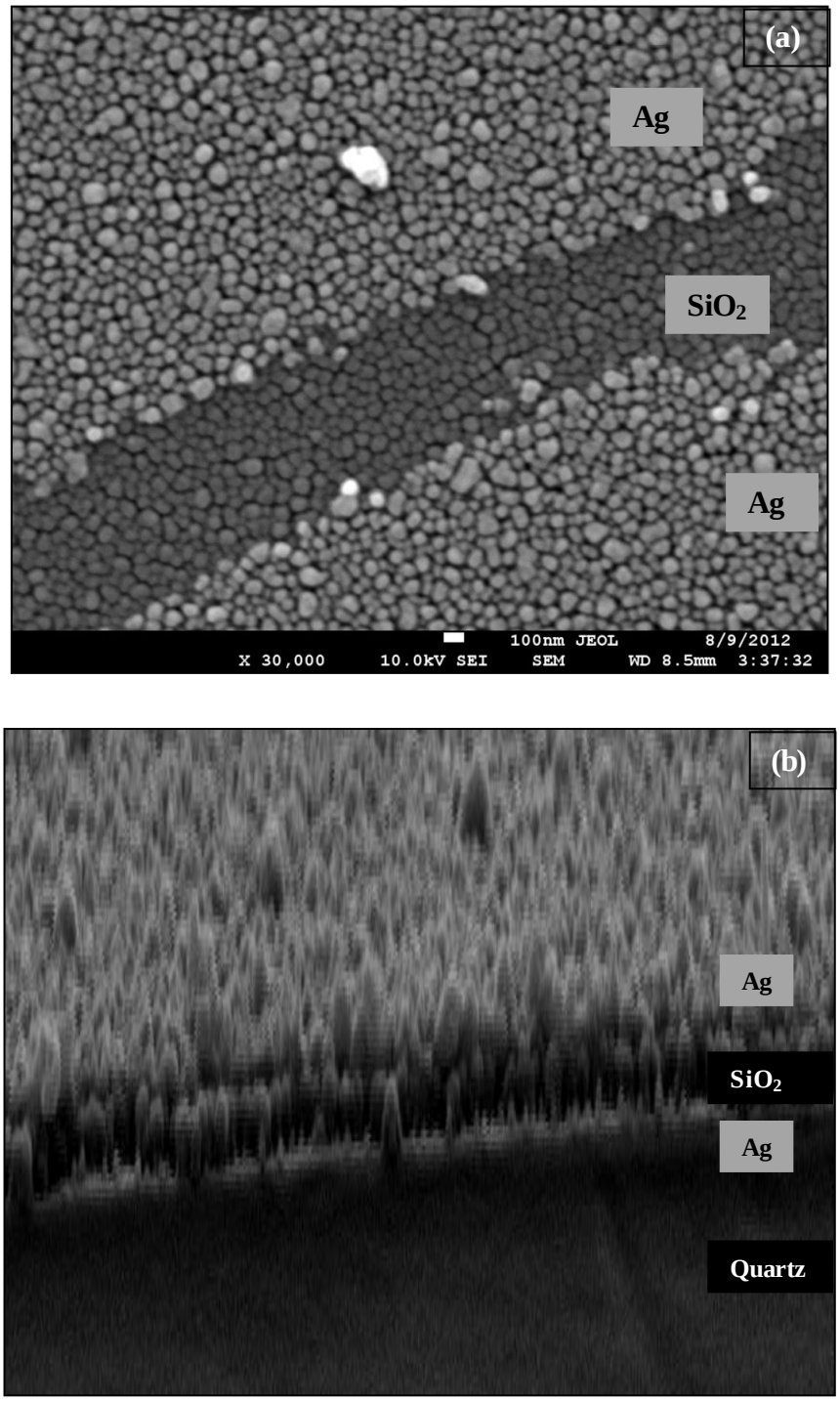

Figure 3.2 The SEM images of $Ag/SiO_2/Ag$ multilayer thin films a) Ag surface of the $Ag/SiO_2/Ag$ thin films b) cross-sectional view of layers of the $Ag/SiO_2/Ag$ thin films.

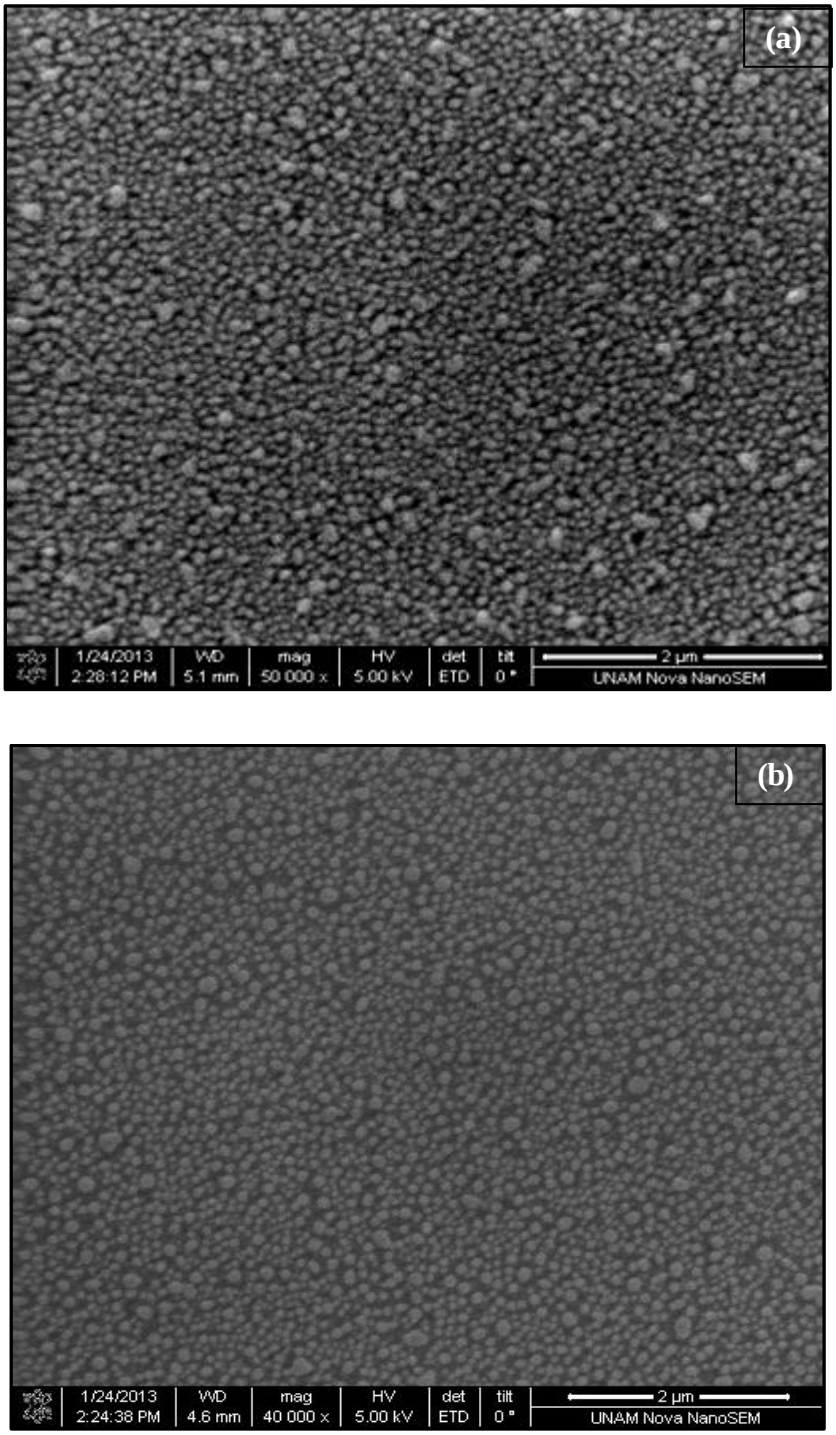

Figure 3.3 The SEM images of $Ag/SiO_2/Ag$ multilayer thin films that have 60 nm SiO_2 thickness at a) 20 ^{0}C and b) 450 ^{0}C.

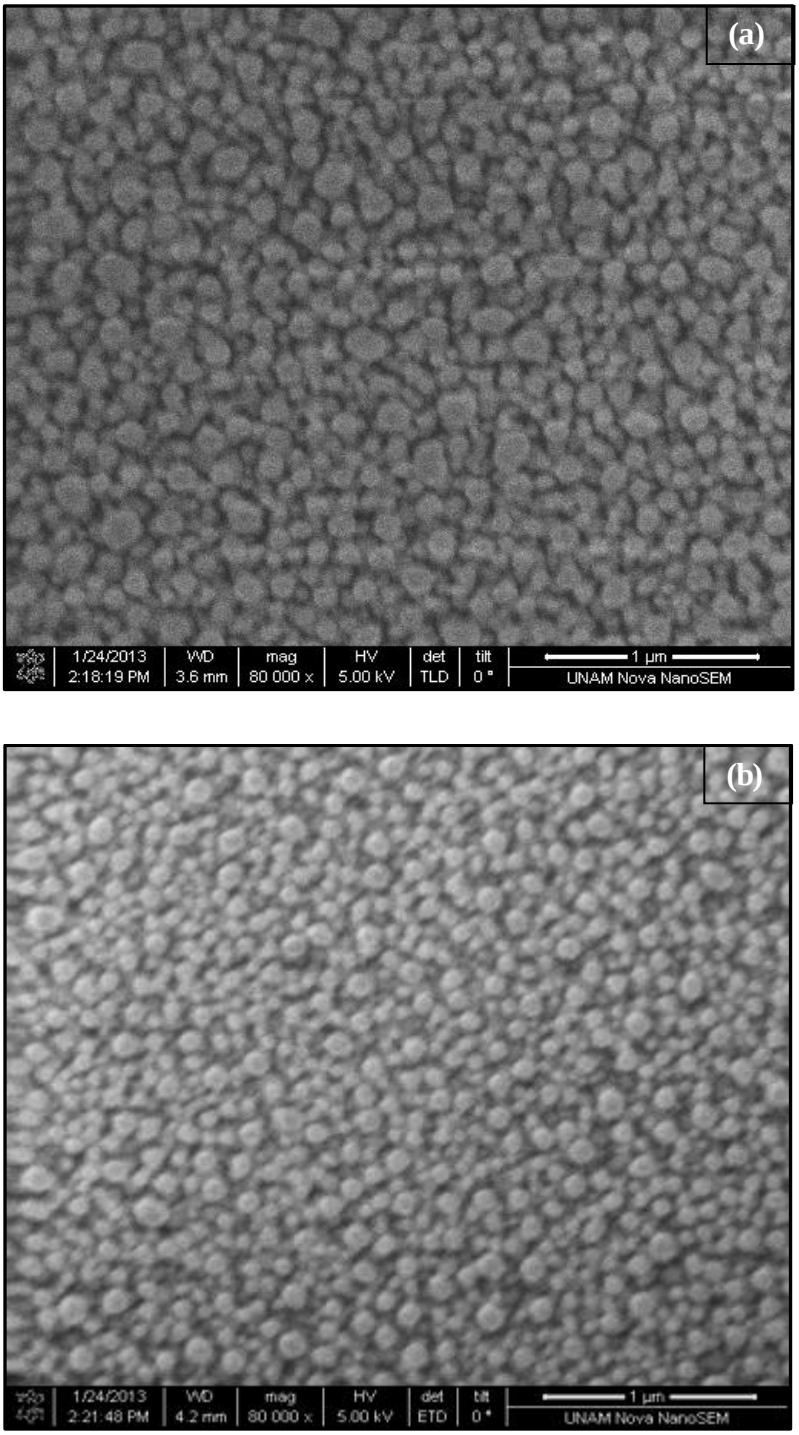

Figure 3.4 The SEM images of $Ag/SiO_2/Ag$ multilayer thin films at 450 ^0C for a) 20 nm and b) 40 nm of SiO_2 thickness.

3.2.2 AFM Measurements

The AFM parameters to obtain the images were carefully set to minimize the pressure of tip on the membranes. A commercial Si tip was used with the nominal radius <10 nm, resonant frequency nominal of 330 kHz, a nominal spring constant of 42 N/m (Contact Cantilever, Nanosensors, Switzerland). 20×20 μm images were acquired at a resolution of 512×512 points within the range of 0.8–1.0 Hz scan rate and were subjected to first-order flattening. Surface roughness was calculated by using the Root Mean Square (RMS), that is, the standard deviation of the Z values within a given area, defined by,

$$\mathrm{RMS} = \sqrt{\frac{\sum_{i=1}^{N}(Z_i - Z_{ave})^2}{N}} \tag{3.1}$$

Where Z_{ave} is the average, Z_i is the current Z value, and N is the number of points within the analyzed area [51]. It was noted that the surface roughness depends on the tortuosity and size of the AFM tip and on the image processing [52] therefore we applied the same procedure for each image.

The surface topography was examined for Ag/SiO_2/Ag multilayer thin films at different SiO_2 thicknesses (20 nm, 40 nm, 60 nm and 120 nm). Hence, Ag clusters were observed on the thin films surface at 20 ^{0}C and 450 ^{0}C. These clusters were shown in Fig. 3.5, Fig. 3.6, Fig. 3.7 and Fig. 3.8.

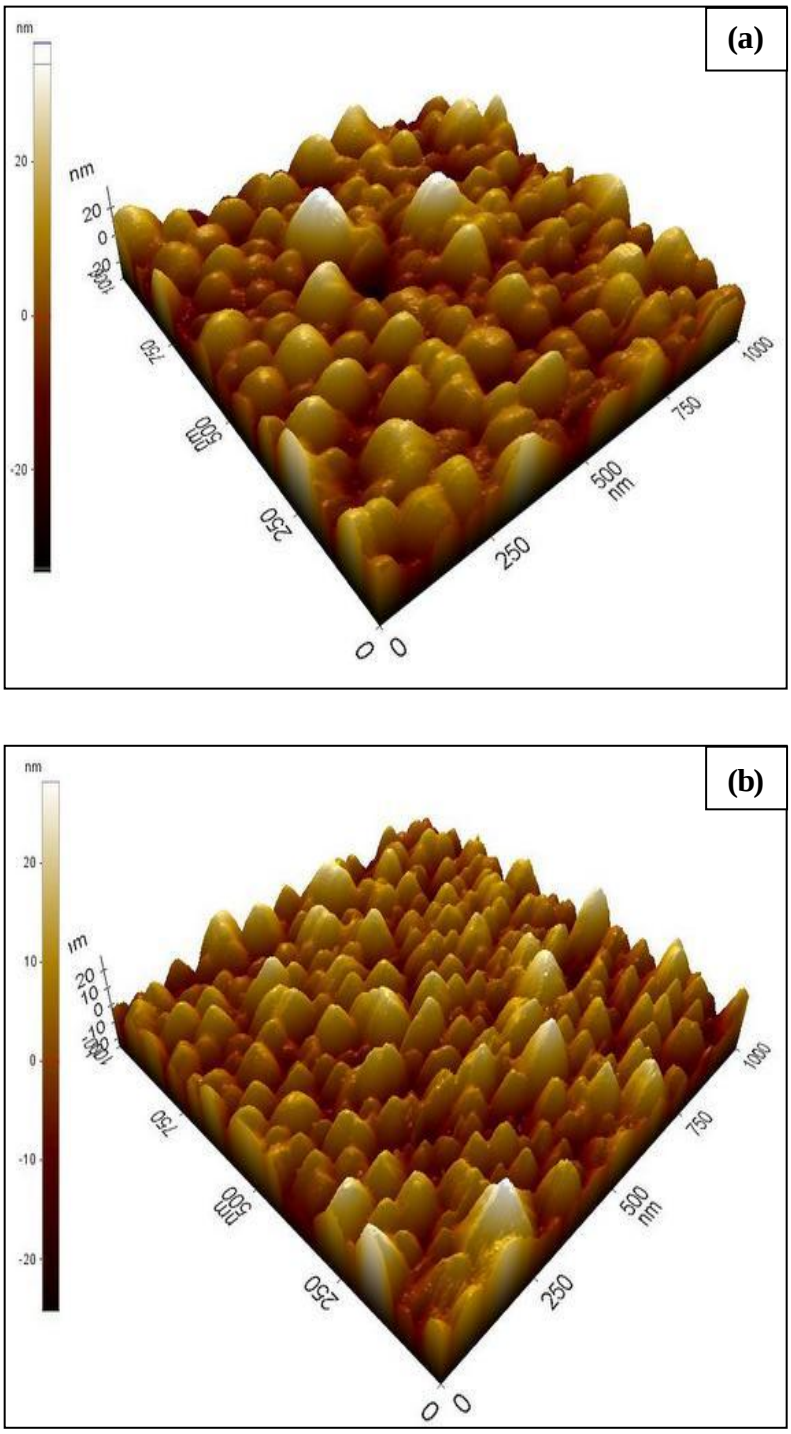

Figure 3.5 AFM images of Ag/SiO_2/Ag thin films that have different SiO_2 thickness at 20°C a) 20nm and b) 40 nm.

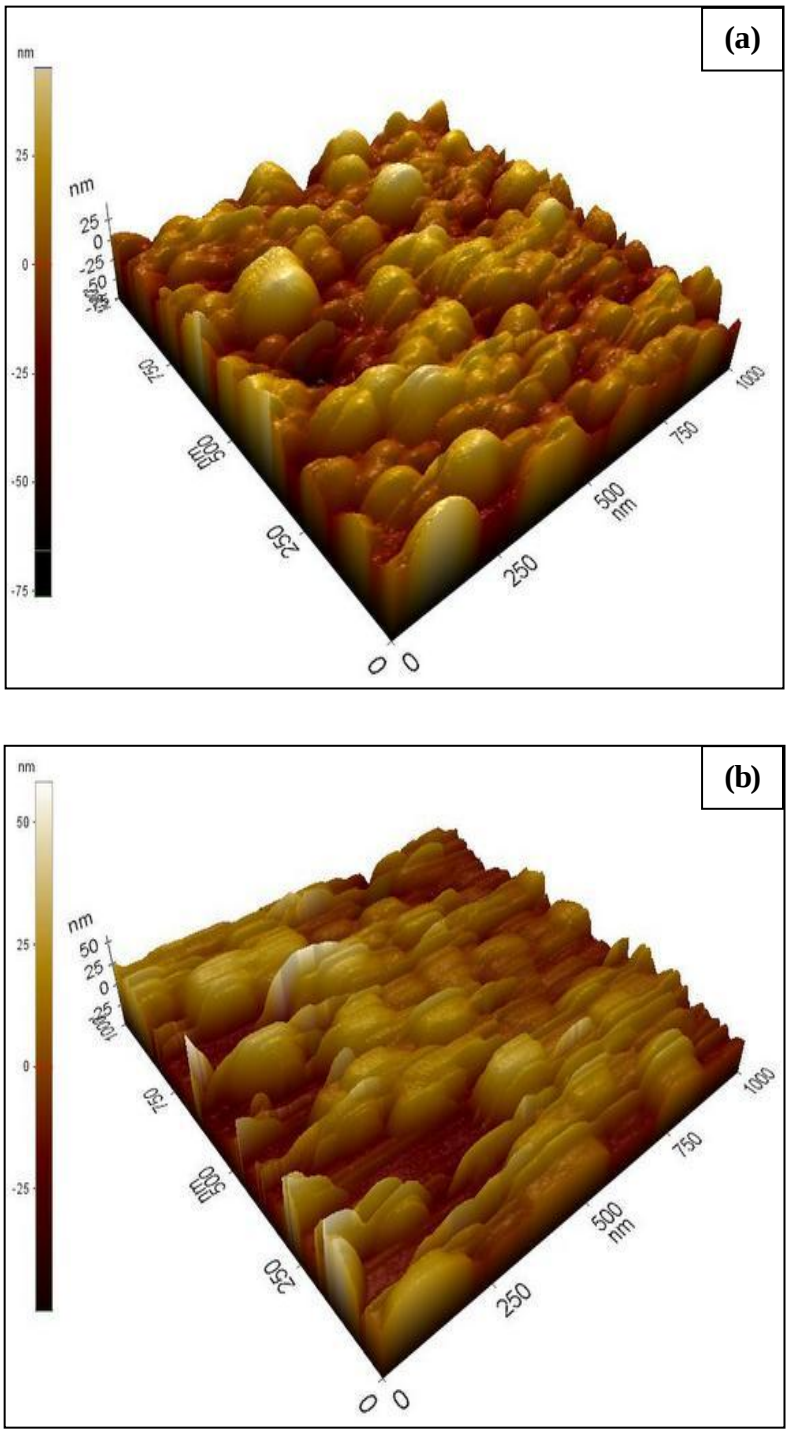

Figure 3.6 AFM images of $Ag/SiO_2/Ag$ thin films that have different SiO_2 thickness at 20°C a) 60 nm and b) 120 nm.

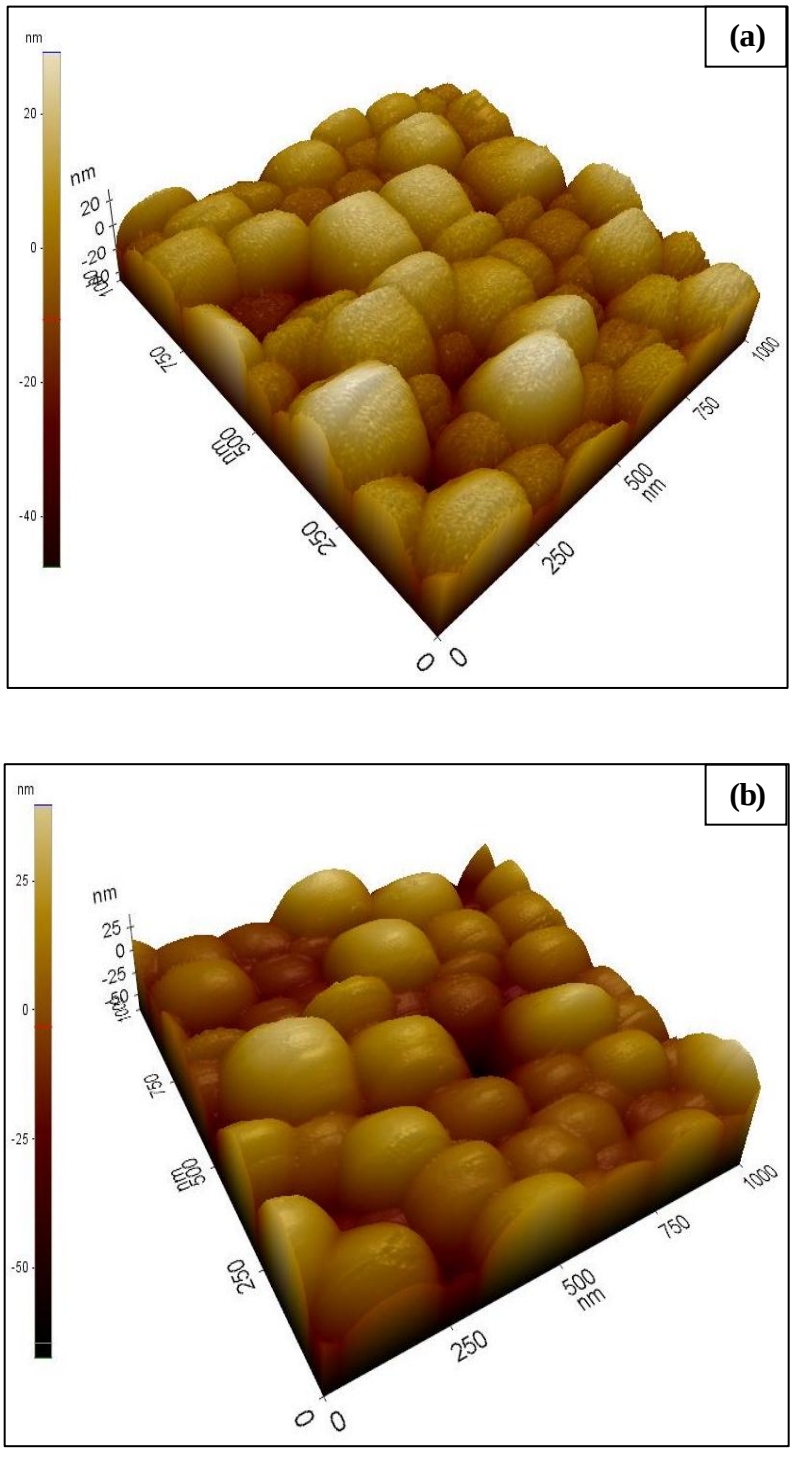

Figure 3.7 AFM images of $Ag/SiO_2/Ag$ thin films at different SiO_2 thickness at 450 °C a) 20 nm and b) 40 nm.

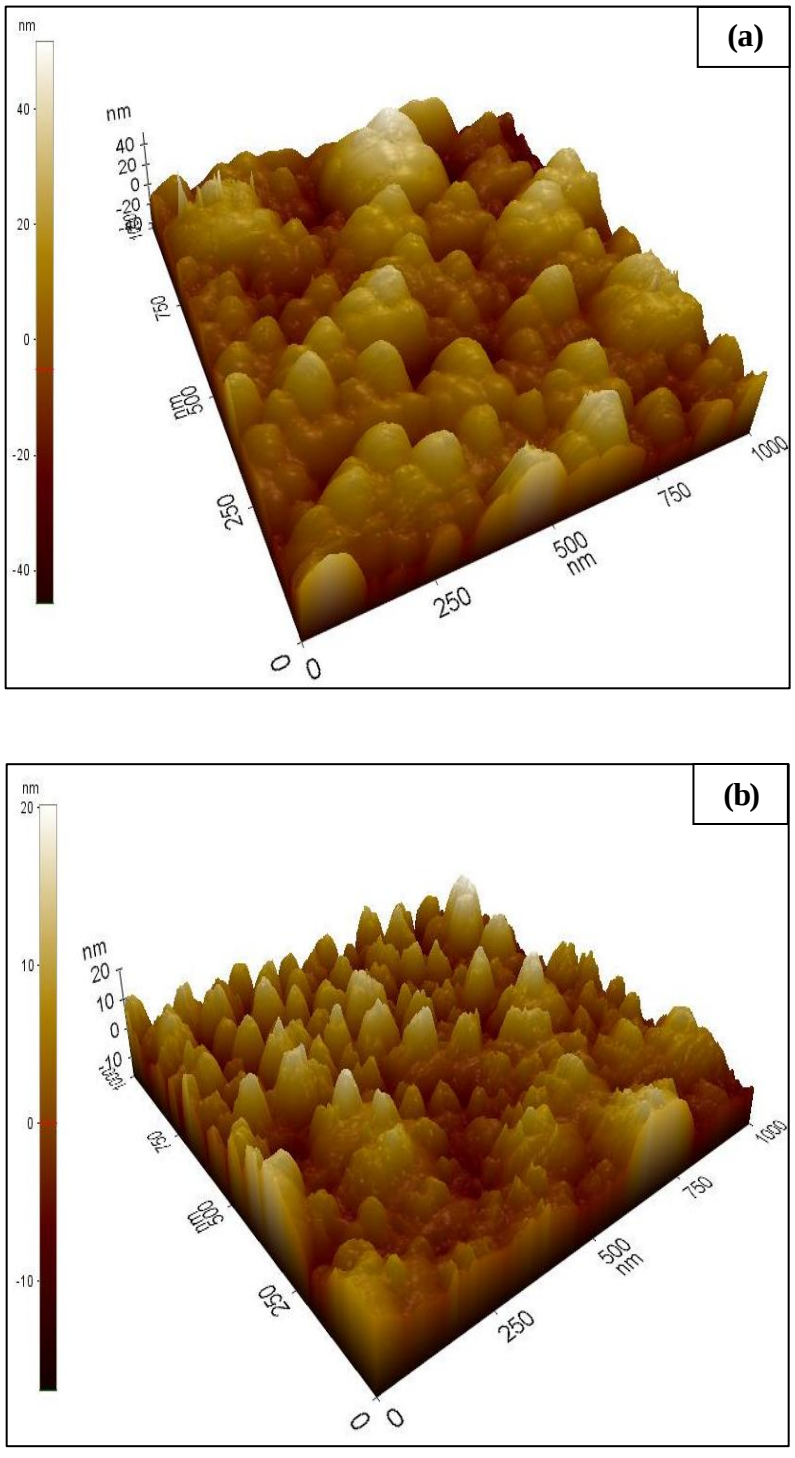

Figure 3.8 AFM images of $Ag/SiO_2/Ag$ thin films at different SiO_2 thickness at 450 °C a) 60 nm and b) 120 nm.

In these clusters, the roughness of the Ag surface was changed with increasing temperature. When the total thickness of thin film is increased, the grains on the surface have large surface energy. The grains tend to aggregate so as to reduce surface energy but increase the surface roughness [53]. For $Ag/SiO_2/Ag$ multilayer thin films, the increase in the roughness of surface was seen uniformly without 20 nm SiO_2 thickness of multilayer thin films.

Table 3.1 Roughness of $Ag/SiO_2/Ag$ multilayer thin film with changing SiO_2 thicknesses of thin films at 20 ^oC.

SiO_2 Thickness of Thin Film (nm)	**Roughness (nm)**
20	16.17
40	4.72
60	6.79
120	14.62

3.3 XRD ANALYSIS

The XRD pattern of the films and annealed films were shown in Fig. 3.9. The annealing treatments were accomplished by using EBD system. Deposited films were annealed for 30 min at 450 °C. Before and after the annealing process, the films are characterized using XRD.

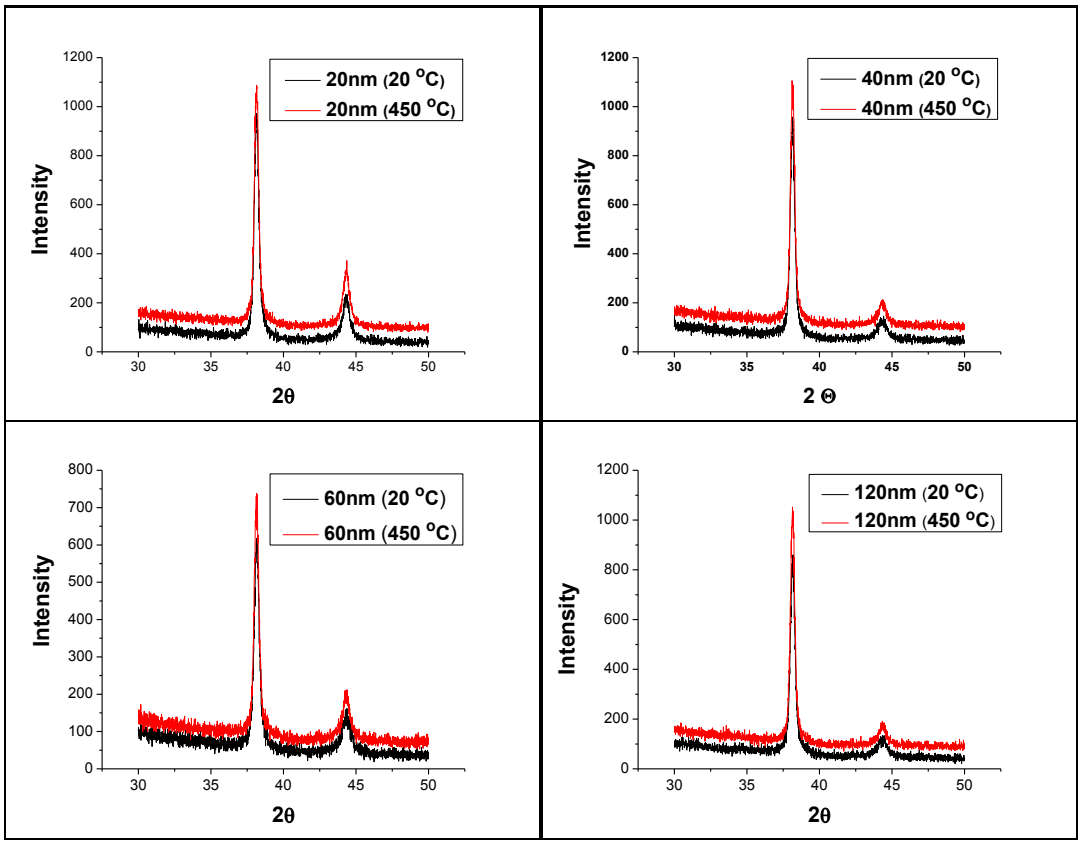

Figure 3.9 XRD spectra of Ag/SiO_2/Ag multilayer substrates for 20 nm, 40 nm, 60 nm and 120 nm of SiO_2 thickness at 20 °C and 450 °C.

Indexing process of powder diffraction pattern was done, Miller indices (h k l) to each peak assigned in first step and the results were shown in Table 3.1. The high intense peak for fcc films is usually (111) reflection, which is observed for the films. The intensity of peaks reflected the high degree of crystalline of the silver multilayer films. However, the diffraction peaks are broad which indicating that the crystallite size is very small. The XRD spectrum confirmed the crystalline structure of silver is face centered cubic (fcc) structure.

The size of Ag nanoparticles was slightly changed with the increasing SiO_2 thicknesses as shown in Table 3.1. The standard strongest peak of silver is observed at 2θ value of 38.3182, this degree corresponds to (111) plane of silver. The experimental diffraction angle (2θ) for (111) plane was observed at 2θ of 38.14. The particle size was determined with two methods: Scherrer Method and Williamson Hall Method.

3.3.1 Scherrer Method

For this thesis, the average particle size was estimated by using Debye-Scherrer Formula [54, 55]:

$$D = \frac{K\lambda}{\beta\cos\theta} \tag{3.2}$$

Where K is a constant equal to 0.94, λ is wavelength of X-Ray CuK_α (0.154 nm), β is FWHM (full width at half maximum), θ is the diffraction angle and D is particle size. The calculated particle size, lattice parameter, FWHM results for different temperatures and SiO_2 thicknesses were shown in Table 3.2. The value of d (the interplanar spacing between the atoms) was calculated using Bragg's Law [56].

$$2d\sin\theta = n\lambda \tag{3.3}$$

Where n = 1, 2, 3...is the degree of the maximum of the total number of diffraction. In most done experiments, n > 1 case to the maxima was observed in very weak intensity and generally, n = 1 case becomes important.

Table 3.2 Crystalline properties calculating by Scherrer method.

Film thickness (nm)	Temperature (˚C)	2θ of the intense peak (nm)	hkl	FWHM of intense peak β	Size of the particle D (nm)	d spacing (nm)	Lattice parameter a (nm)
20	20	38,15	(111)	0,0069	21,91	0,236	0,408
	450	38,15	(111)	0,0066	23,21	0,236	0,408
40	20	38,14	(111)	0,0069	22,23	0,236	0,408
	450	38,15	(111)	0,0066	23,21	0,236	0,408
60	20	38,15	(111)	0,0078	19,73	0,236	0,408
	450	38,15	(111)	0,0072	20,27	0,236	0,408
120	20	38,14	(111)	0,0071	21,72	0,236	0,408
	450	38,14	(111)	0,0067	22,86	0,236	0,408

3.3.2 Williamson-Hall Method

Strain induced broadening arising from the crystal imperfections and distortions are related by $\varepsilon \approx \beta / \tan\theta$. The dependency on the diffraction angle θ is a remarkable property for Scherrer equation. Size and strain broadening are related with total integral breadth of a Bragg peak represented by different approaches [57]. In addition Scherrer equation and $\varepsilon \approx \beta / \tan\theta$ results in following equations:

$$D = \frac{K\lambda}{\beta \cos\theta} + 4\varepsilon \tan\theta \tag{3.4}$$

$$\beta \cos\theta = \frac{K\lambda}{D} + 4\varepsilon \sin\theta \tag{3.5}$$

In this thesis, Williamson-Hall method was also used to find the crystallite size of Ag nanoparticles on thin films. The Williamson-Hall method may be assumed as three different models which are uniform deformation model (UDM), uniform deformation stress model (USDM) and uniform deformation energy density model (UDEDM). In the Eq. (3.5), the using method represents the UDM, where the strain was assumed to be uniform in all crystallographic directions. This means that all material properties are independent of the direction through the done experiment. The term ($\beta\cos\theta$) was plotted with respect to ($4\sin\theta$) for Ag nanorods. From providing this graph, the slope and y-intersect of the fitted line represent strain and $\beta\cos\theta$ which is used to calculate crystallite size, respectively. The results of the UDM analysis for the Ag nanorods at 20°C and annealed 450°C were shown in Fig. 3.10 and Fig. 3.11.

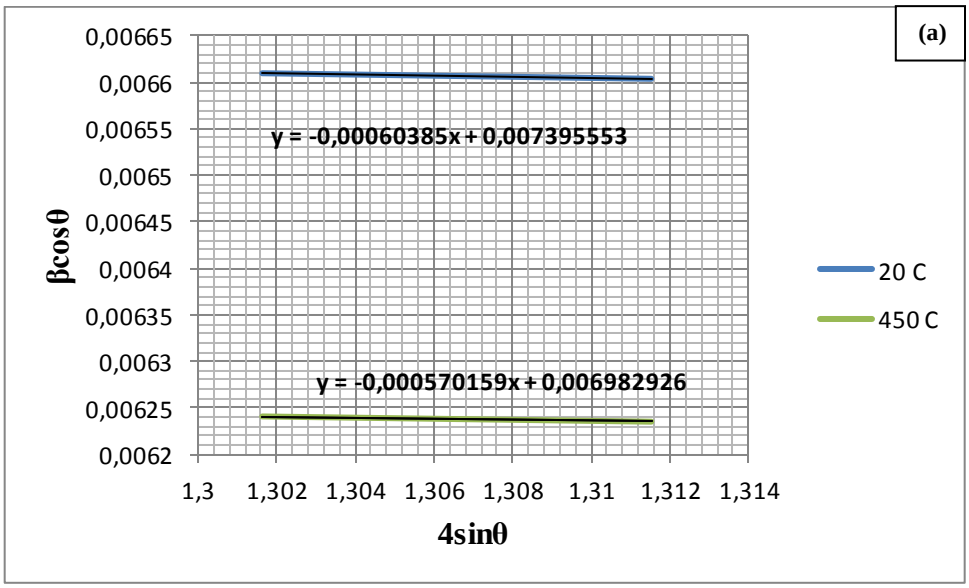

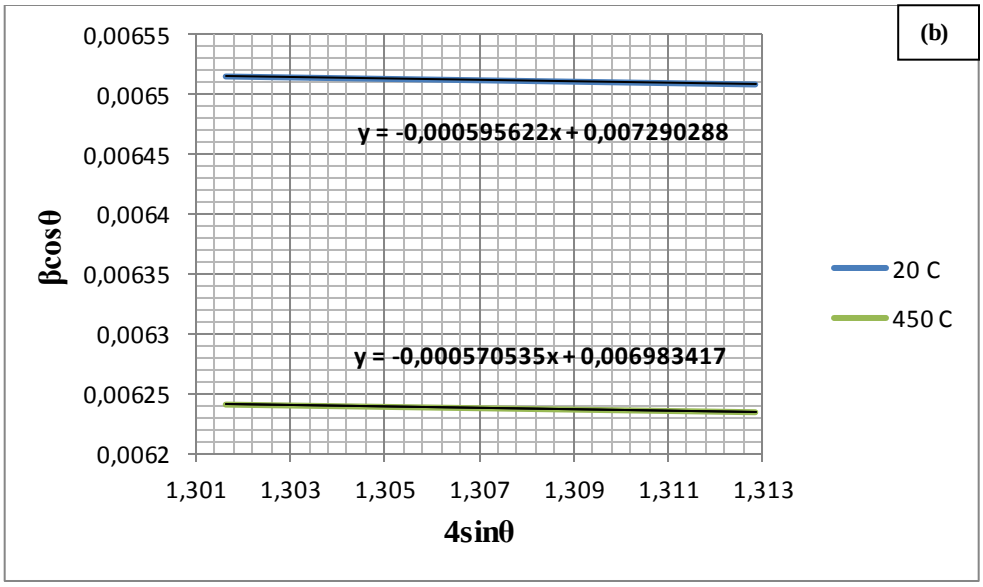

Figure 3.10 The W-H analyses of multilayer films with different SiO_2 thicknesses a) 20 nm and b) 40 nm at 20°C and annealed 450°C for UDM.

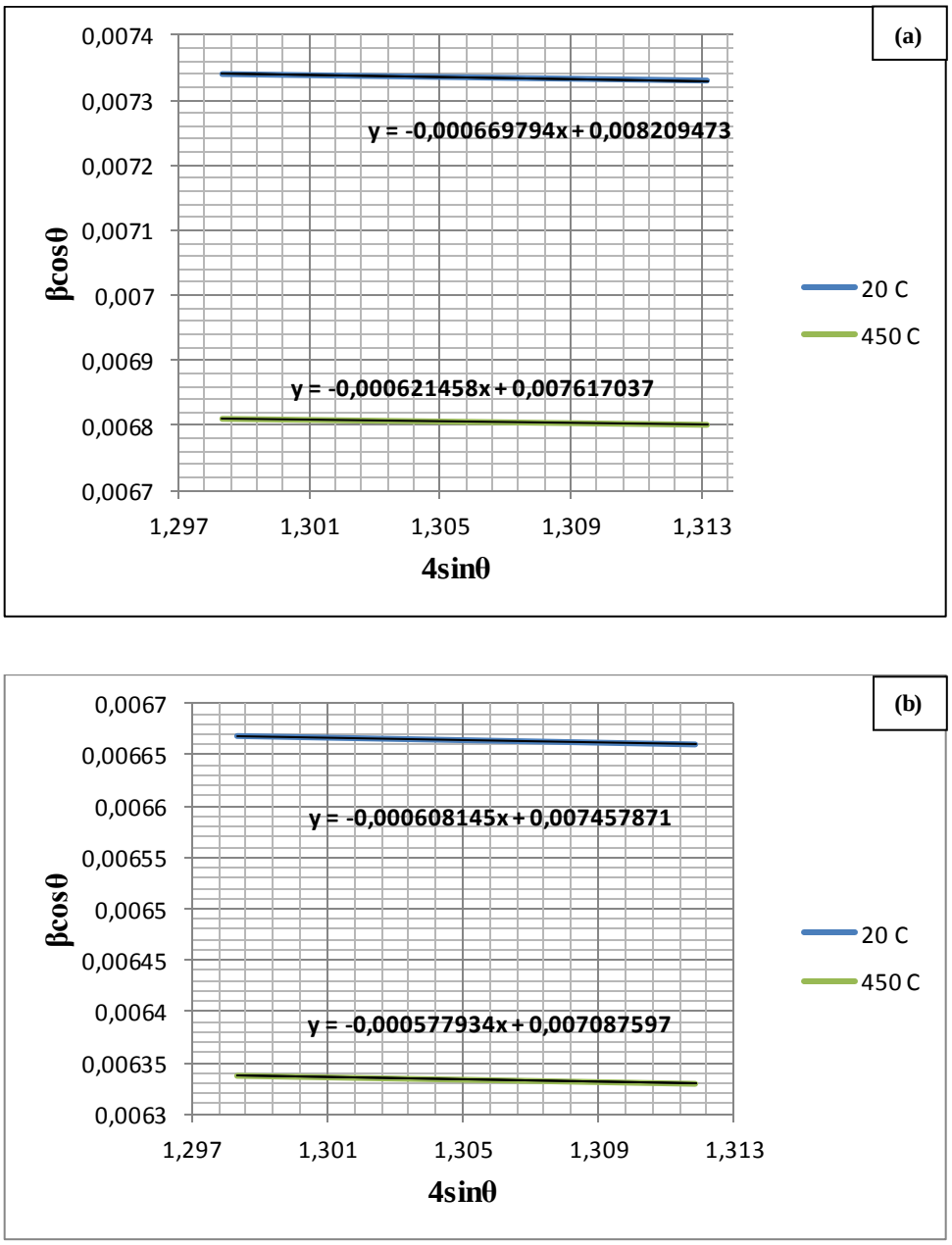

Figure 3.11 The W-H analyses of multilayer films with different SiO_2 thicknesses a) 60 nm and b) 120 nm at 20°C and annealed 450°C for UDM.

In the USDM, according to Hooke's law, the relation which has linear proportionality between strain and stress as given by $\sigma = Y\varepsilon$ where σ is the stress of the crystal and Y is the modulus of elasticity (Young's modulus). This equation is an approximation that is only valid for an importantly small strain. If the small strain is present in the Ag nanoparticles, the Hooke's law can be used. The particles deviate from this linear proportionality with a more increase in strain. Eq. (3.6) is derived with applying the Hooke's law approximation to Eq. (3.5):

$$\beta \cos\theta = \frac{K\lambda}{D} + \frac{4\sigma \sin\theta}{Y_{hkl}} \tag{3.6}$$

Young's modulus (Y_{hkl}) is assumed as uniform in all crystallographic directions for fcc Ag nanorods which have isotropic nature of crystal was calculated as 83 GPa [58]. Plots were drawn with $(4 \sin\theta)/Y_{hkl}$ on the x-axis and $\beta_{hkl}\cos\theta$ on the y-axis for the Ag nanorods annealed at different temperatures. The USDM plots for Ag-nanorods at 20°C and annealed 450 °C was shown in Fig. 3.12 and Fig. 3.13.

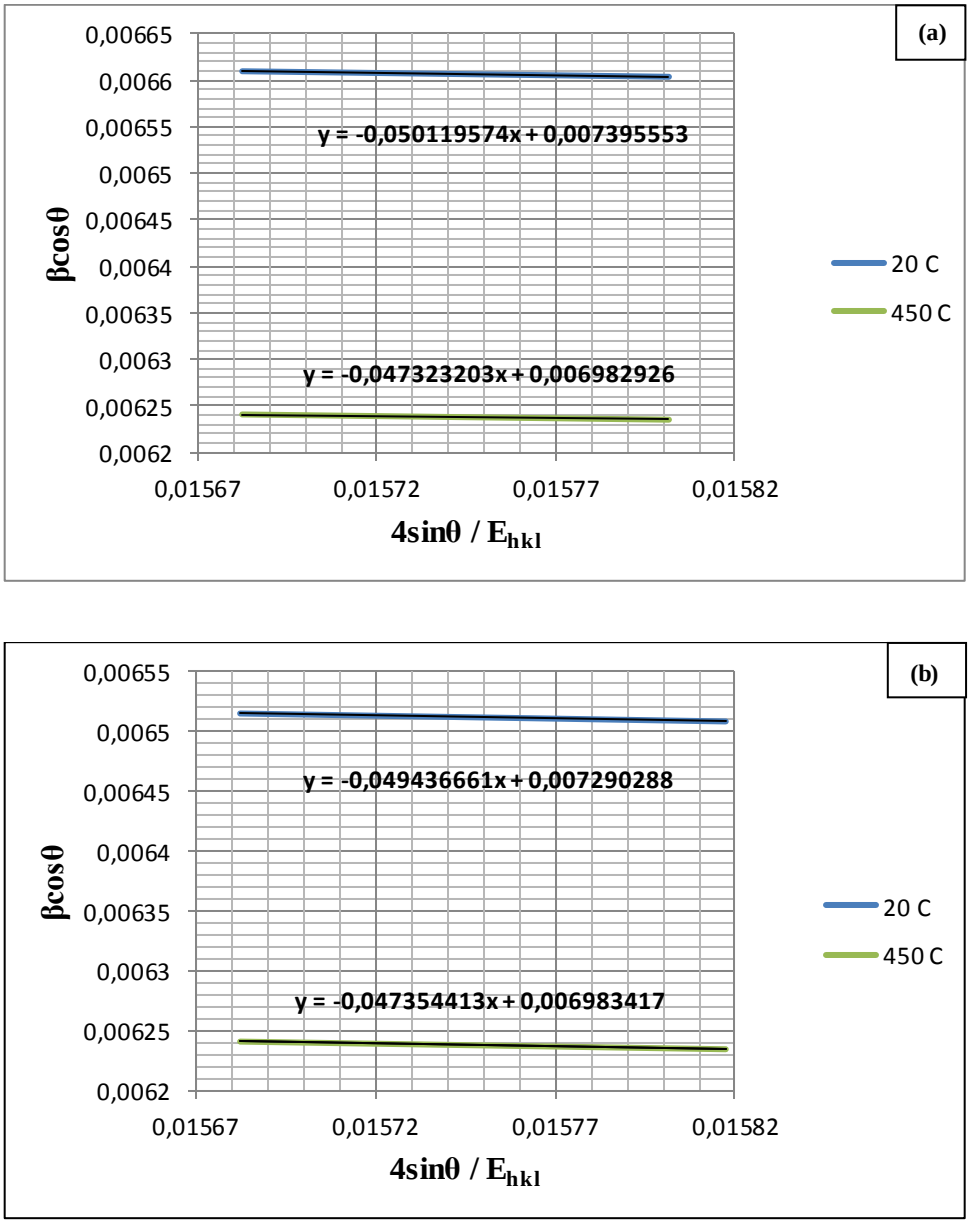

Figure 3.12 The W-H analyses of multilayer films with different SiO_2 thicknesses a) 20 nm and b) 40 nm at 20 °C and annealed 450°C for USDM.

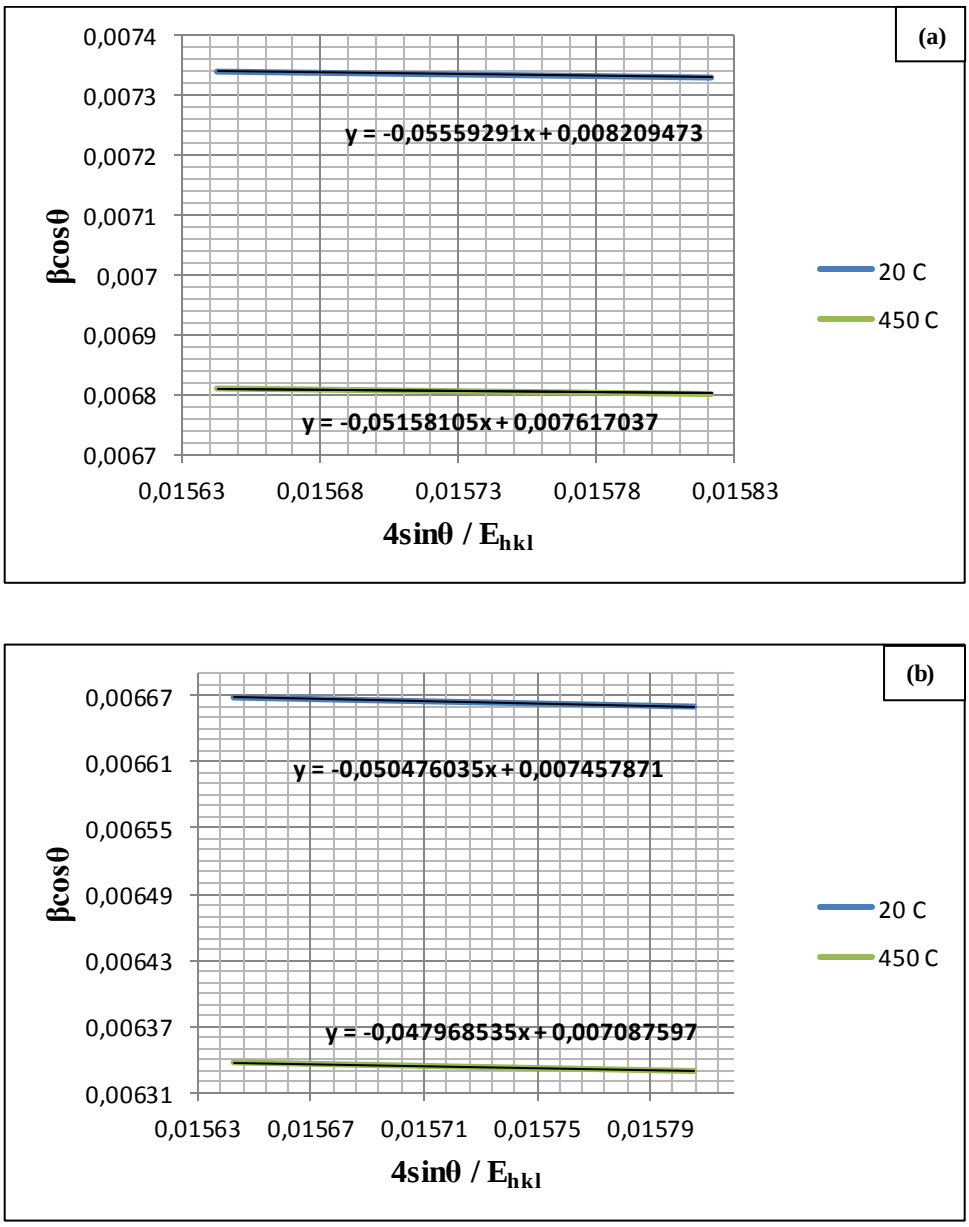

Figure 3.13 The W-H analyses of multilayer films with different SiO_2 thicknesses a) 60 nm and b) 120 nm at 20 °C and annealed 450°C for USDM.

The other method is UDEDM that can be used to determine the energy density of a crystal. In Eq. (3.6), the crystals are assumed to have an isotropic nature. However, in many cases, the assumption of homogeneity and isotropy is sometimes not justified. Moreover, the constants of proportionality associated with the stress-strain relation are no longer independent when the strain energy density u is considered. For an elastic system, the energy density u can be calculated from $u = (\sigma^2 Y_{hkl})/2$ by using Hooke's Law. Then Eq. (3.6) which is related to the energy and strain relation can be rewritten as:

$$\beta \cos\theta = \frac{K\lambda}{D} + 4\sin\theta \left(\frac{2u}{Y_{hkl}}\right)^{1/2} \tag{3.7}$$

Plots of $\beta(hkl)\cos\theta$ versus $4\sin\theta(2u/Y_{hkl})^{1/2}$ were constructed and the data fitted to lines. The anisotropic energy density (u) was calculated from the slope of these lines, and $\beta\cos\theta$ which is used to calculate crystallite size from the y-intercept. The UDEDM plots for Ag- nanorods were at 20 °C and annealed 450 °C was shown in Fig. 3.14 and Fig. 3.15.

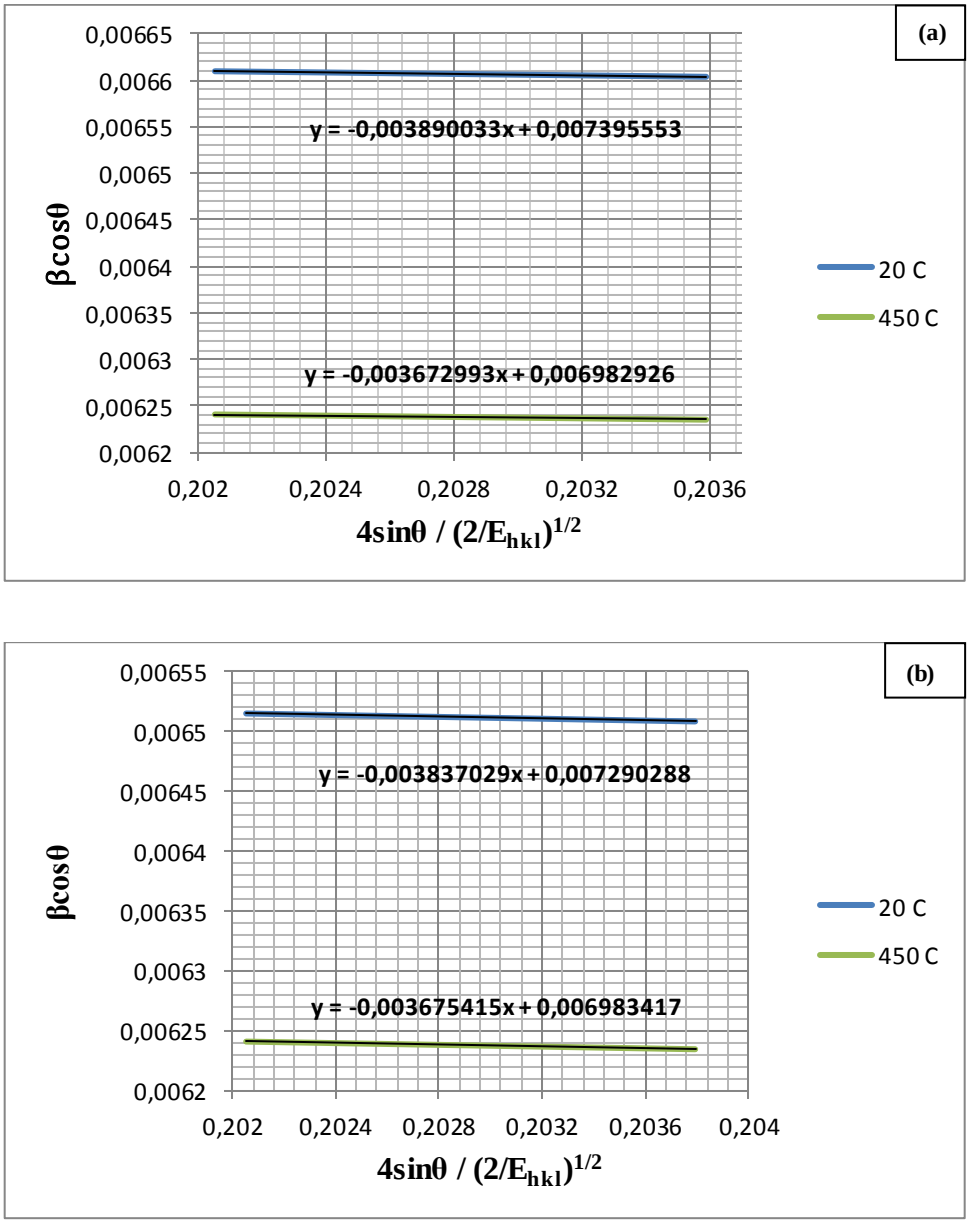

Figure 3.14 The W-H analyses of multilayer films with different SiO_2 thicknesses a) 20 nm and b) 40 nm at 20 °C and annealed at 450°C for UDEDM.

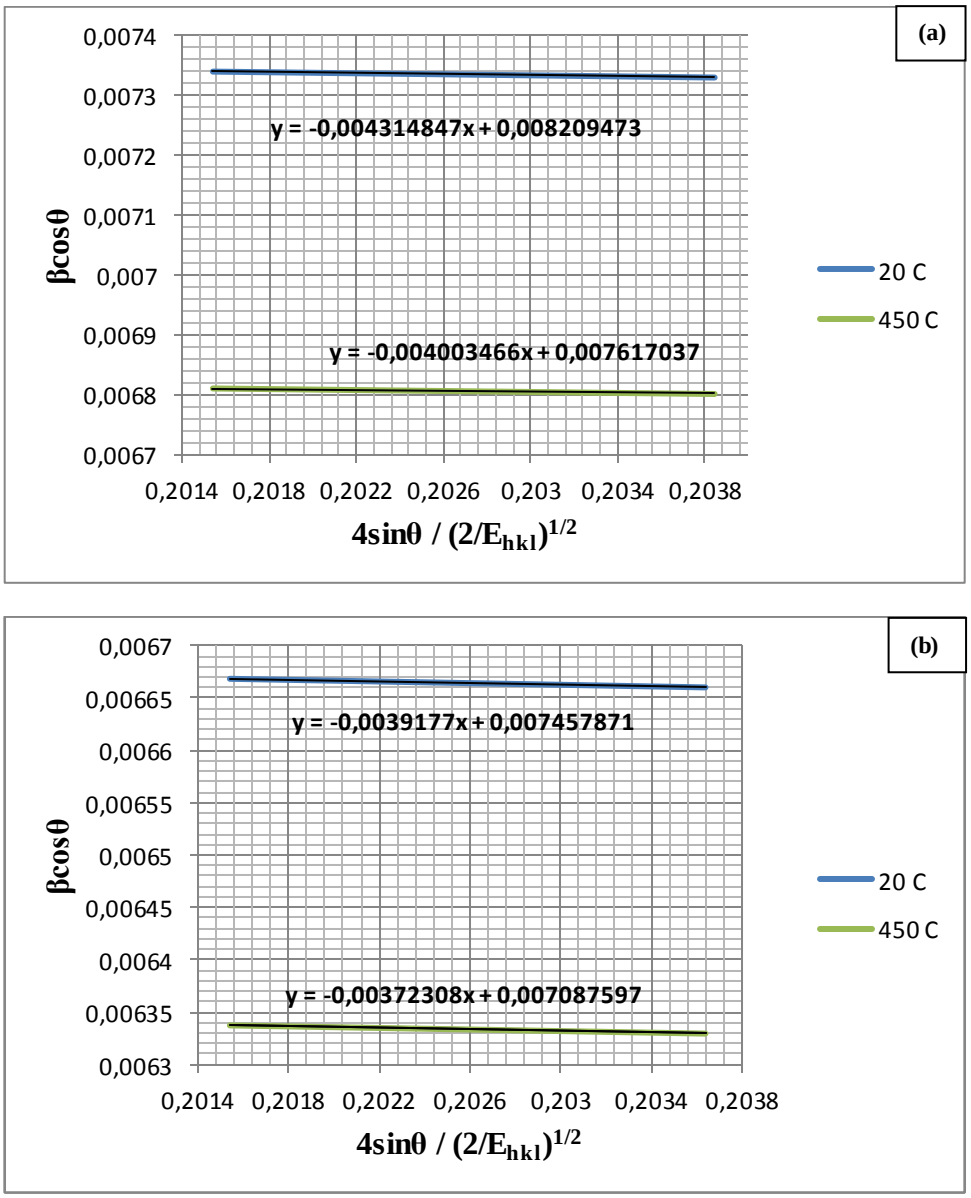

Figure 3.15 The W-H analyses of multilayer films with different SiO_2 thicknesses a) 60 nm and b) 120 nm at 20 °C and annealed at 450°C for UDEDM.

The results obtained from the UDM, USDM and UDEDM were summarized in Table 3.3.

Table 3.3 Geometric parameters of multilayer Ag films with different SiO_2 thicknesses before (at 20 °C) and after annealing (at 450 °C).

Thick. (nm)	Temp. (°C)	Williamson-Hall Method									
		UDM			USDM			UDEDM			
		ε x10^{-3}	σ (MPa)	D (nm)	ε x10^{-3}	σ (MPa)	D (nm)	ε x10^{-3}	σ (MPa)	U (kJm^{-3})	D (nm)
20	20	0,604	50,13	19,56	0,604	50,13	19,56	0,604	50,12	15,13	19,56
	450	0,570	47,31	20,74	0,570	47,34	20,74	0,570	47,29	13,47	20,74
40	20	0,595	49,39	19,83	0,595	49,42	19,83	0,596	49,48	14,75	19,83
	450	0,570	47,31	20,74	0,570	47,34	20,74	0,570	47,29	13,47	20,74
60	20	0,671	55,69	17,63	0,670	55,65	17,63	0,670	55,64	18,65	17,63
	450	0,622	51,63	19,05	0,622	51,64	19,05	0,621	51,54	16,00	19,05
120	20	0,609	50,55	19,43	0,609	50,57	19,43	0,605	50,25	15,21	19,43
	450	0,579	48,06	20,45	0,579	48,05	20,45	0,577	47,93	13,84	20,45

3.4 OPTICAL PROPERTIES OF THIN FILMS

3.4.1 UV-Vis Spectroscopic Measurements

There is an effect as called conjugation that causes the absorption. For this effect, there are two cases: In the first case, the energy level of bonding electrons (main energy level) is more stable than energy level of nonbonding electrons (excited energy level) and their energy level drops more with respect to nonbonding electrons energy. This leads to shift the absorption in the high energy region (low λ value). This is called as blue shift. For the second case, if the energy level of nonbonding electrons (excited energy level) is more stable than energy level of bonding electrons (main energy level). The energy level of nonbonding electrons drops more according to bonding electrons

energy. This effect leads to shift the absorption in the low energy region (high λ value). This is called as red shift [25-29]. The UV-Vis spectra of $Ag/SiO_2/Ag$ multilayer thin films were shown in Fig. 3.16.

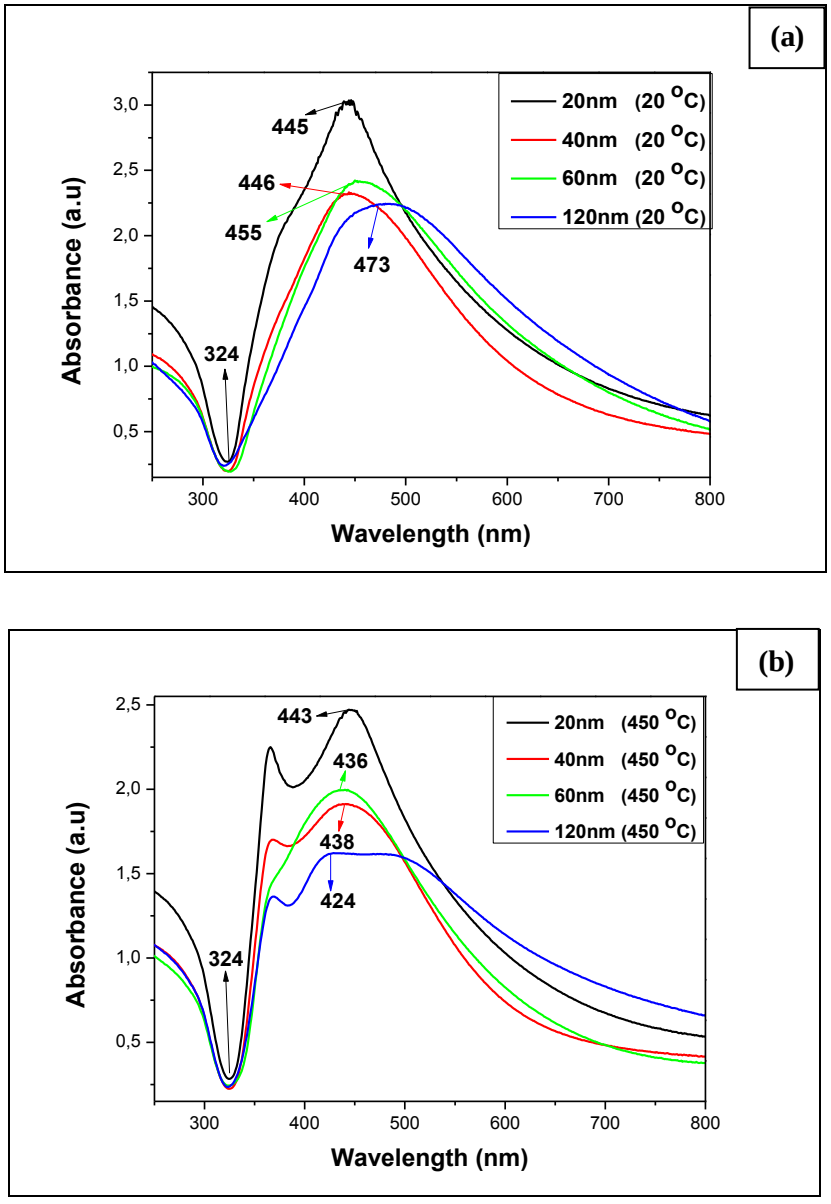

Figure 3.16 UV-Vis spectra of $Ag/SiO_2/Ag$ thin films for changing SiO_2 thickness as 20 nm, 40 nm, 60 nm and 120 nm at a) 20 °C and b) 450 °C.

In this thesis; the surface plasmon peaks of produced thin films shifted to the high wavelengths (red-shifts).The UV-Vis spectroscopy results were appropriate to the

literature values. Increasing SiO_2 thicknesses contribute to retardation effect. The red-shift was shown in the UV-Vis spectra of $Ag/SiO_2/Ag$ thin films that have the different SiO_2 thicknesses as 20 nm, 40 nm, 60 nm and 120 nm.

The UV-Vis spectra for the $Ag/SiO_2/Ag$ multilayer thin films have a plasmon band at 445 nm, 446 nm, 455 nm and 473 nm as shown in Fig. 3.16 a) at 20 ^oC for 20 nm, 40 nm, 60 nm and 120 nm of SiO_2 thickness. The plasmon band of $Ag/SiO_2/Ag$ thin films belonged to transverse plasmon band at 364 nm, 365 nm, 367 nm, 368 nm and second plasmon band belonged to longitudinal plasmon band at 443 nm, 438 nm, 436 nm and 424 nm as shown in Fig. 3.16 b) for different SiO_2 thickness as 20 nm, 40 nm, 60 nm and 120 nm, respectively at 20 ^oC. The interband transition of multilayer thin films was at 324 nm.

3.5 SERS MEASUREMENTS

The SERS activities were tested with Rhodamine 6G (R6G) molecule which was a commonly used SERS probe [59-63]. The structural formula was displayed in Fig. 3.17.

The different concentration of Rhodamine 6G (R6G) molecules as 10^{-3} M, 10^{-6} M, 10^{-7} M, 10^{-8} M and 10^{-9} M were prepared for SERS measurements. Initially, 10^{-3} M of R6G was prepared by solving 0.0479 g of R6G that has molecular weight as 479,01 g/mol in 100 ml distilled water. The other concentration of R6G solutions were prepared by diluting of 10^{-3}M of R6G solution. R6G dye molecules were absorbed on the surface of multilayer SERS-active substrate that was $Ag/SiO_2/Ag$ thin film.

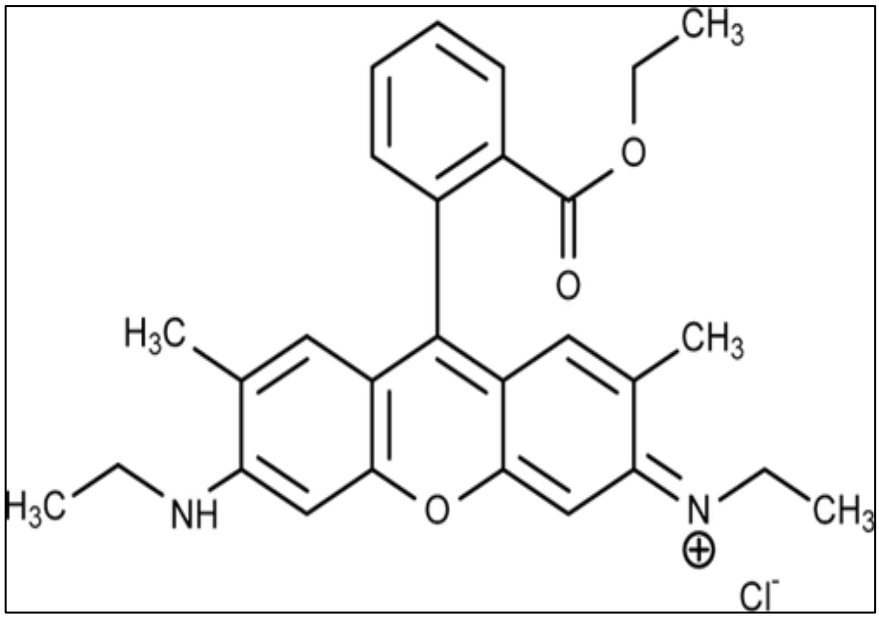

Figure 3.17 Chemical structure of R6G molecule.

The R6G solution was prepared in concentration of 0.1 μM. This solution was dropped onto the prepared SERS active substrates and their Raman spectra of R6G on each film were recorded using Raman microscope. The Raman intensity of R6G on SERS substrate is drastically bigger than its Raman intensity on glass substrate. The SERS and Non SERS spectra of R6G were shown in Fig. 3.18. The increase in intensity was in agreement with the reported SERS spectra recorded on various rough metals [64-66]. Table 3.4 lists the characteristic Raman band and their assignments.

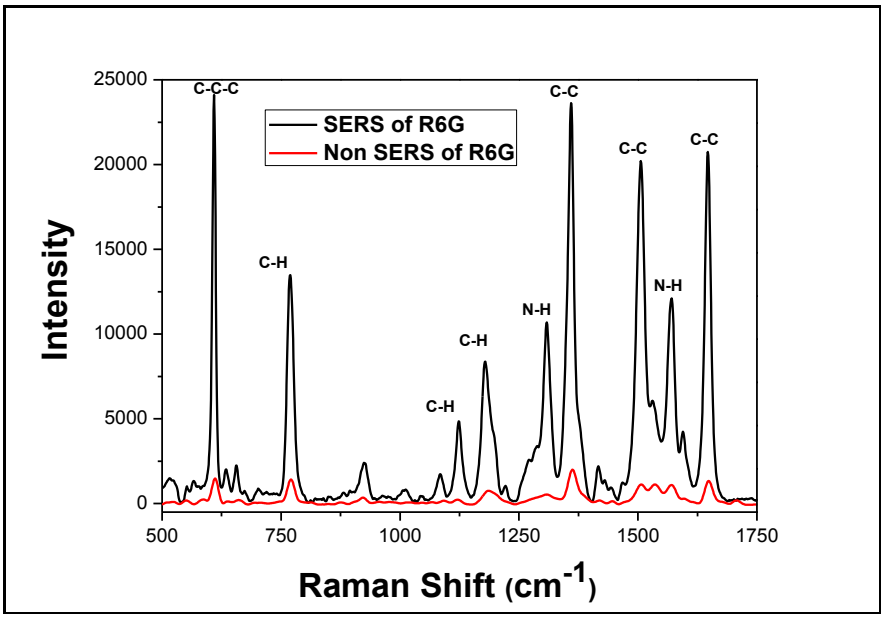

Figure 3.18 Raman and SERS spectrum of R6G.

The Raman spectra of the 10^{-7} M R6G molecules on the $Ag/SiO_2/Ag$ multilayer plasmonic substrates that have different SiO_2 thicknesses at 20 ^0C and 450 ^0C were shown in the Fig. 3.19 and Fig.3.20.

Table 3.4 Vibration modes and their Raman shifts.

Raman Shift Location (cm^{-1})	Assignments
609	C-C-C ring in-plane vibration mode
769	C-H out-of-plane bending mode
1121	C-H in-plane bending mode
1182	C-H in-plane bending mode
1307	N-H in-plane bending mode
1360	C-C stretching mode
1505	C-C stretching mode
1569	N-H in-plane bending mode
1645	C-C stretching mode

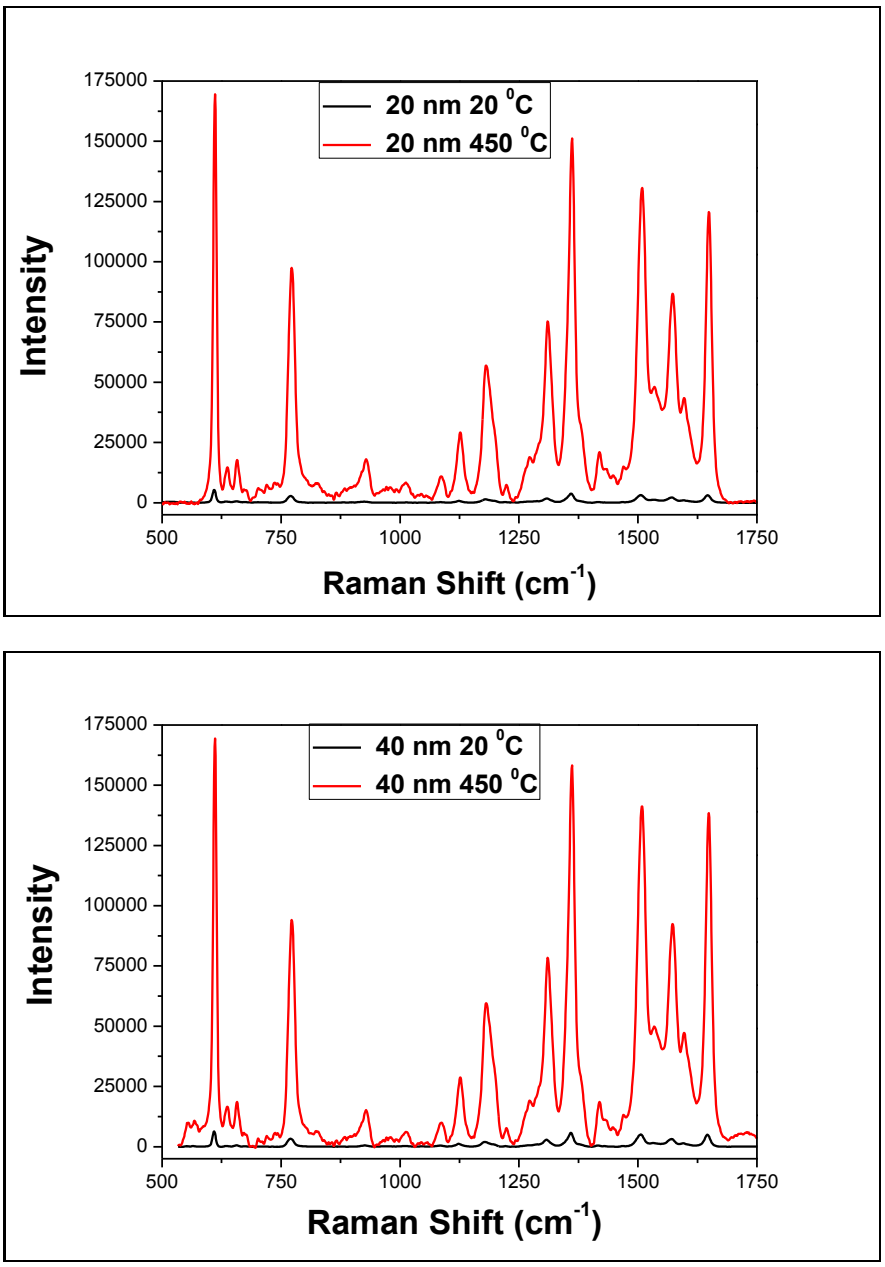

Figure 3.19 The Raman spectra of 10^{-7} M R6G molecules on the $Ag/SiO_2/Ag$ multilayer thin films that have different SiO_2 thicknesses as 20 nm and 40 nm at 20 ^{0}C and 450 ^{0}C.

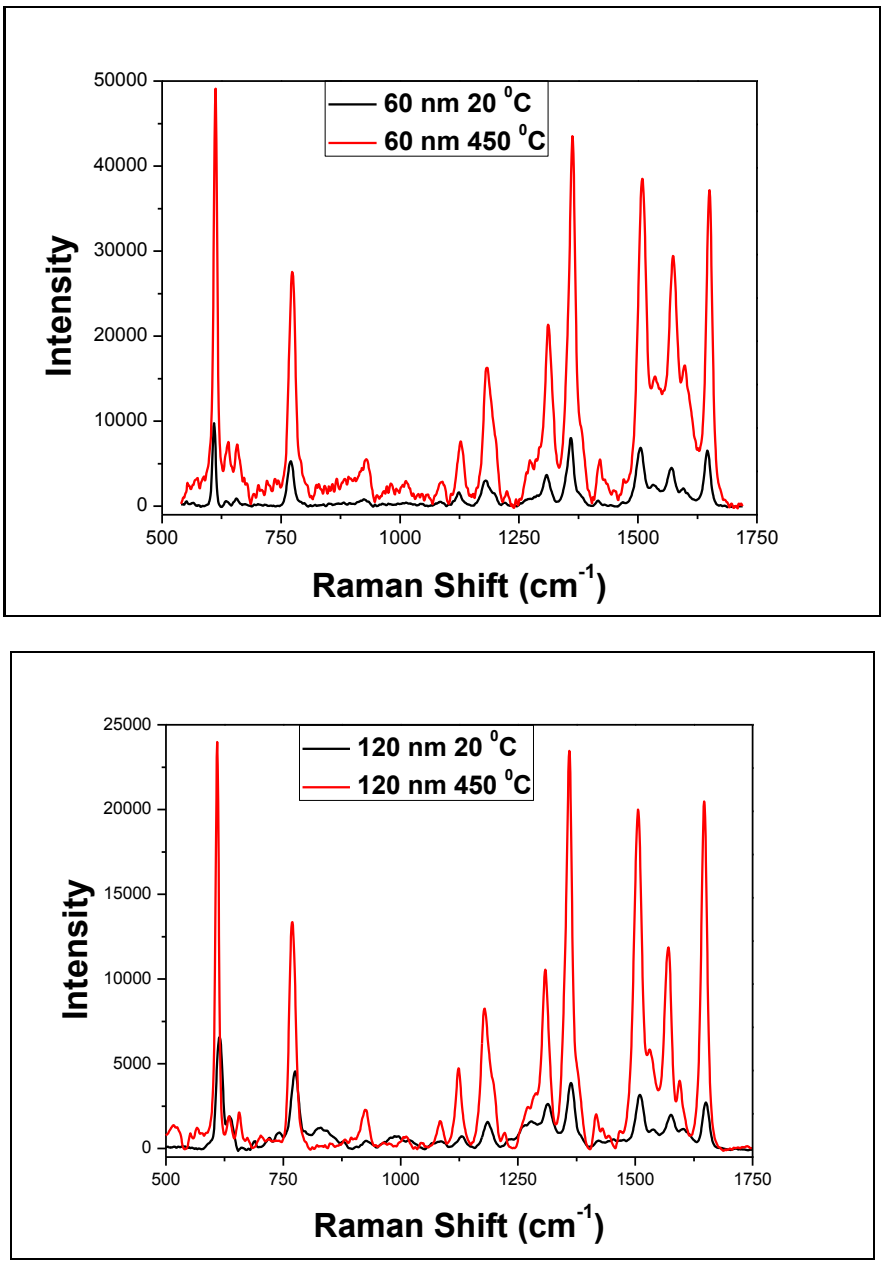

Figure 3.20 The Raman spectra of 10^{-7} M R6G molecules on the $Ag/SiO_2/Ag$ multilayer thin films that have different SiO_2 thicknesses as 60 nm and 120 nm at 20 ^0C and 450 ^0C.

According to Fig. 3.19 and Fig. 3.20, the Raman intensities of the 10^{-7} M R6G molecules on the $Ag/SiO_2/Ag$ multilayer thin films that have different SiO_2 thicknesses were increased after annealing the films at 450 ^{0}C. In order to investigate the repeatability of SERS measurements, 11 spectra on the SERS substrate which has 120 nm thickness of SiO_2 were recorded from different locations on the substrate. The image of R6G on the SERS substrate was shown in the Fig. 3.21 (a). The spectra of R6G taken different points were shown in Fig. 3.21 (b).

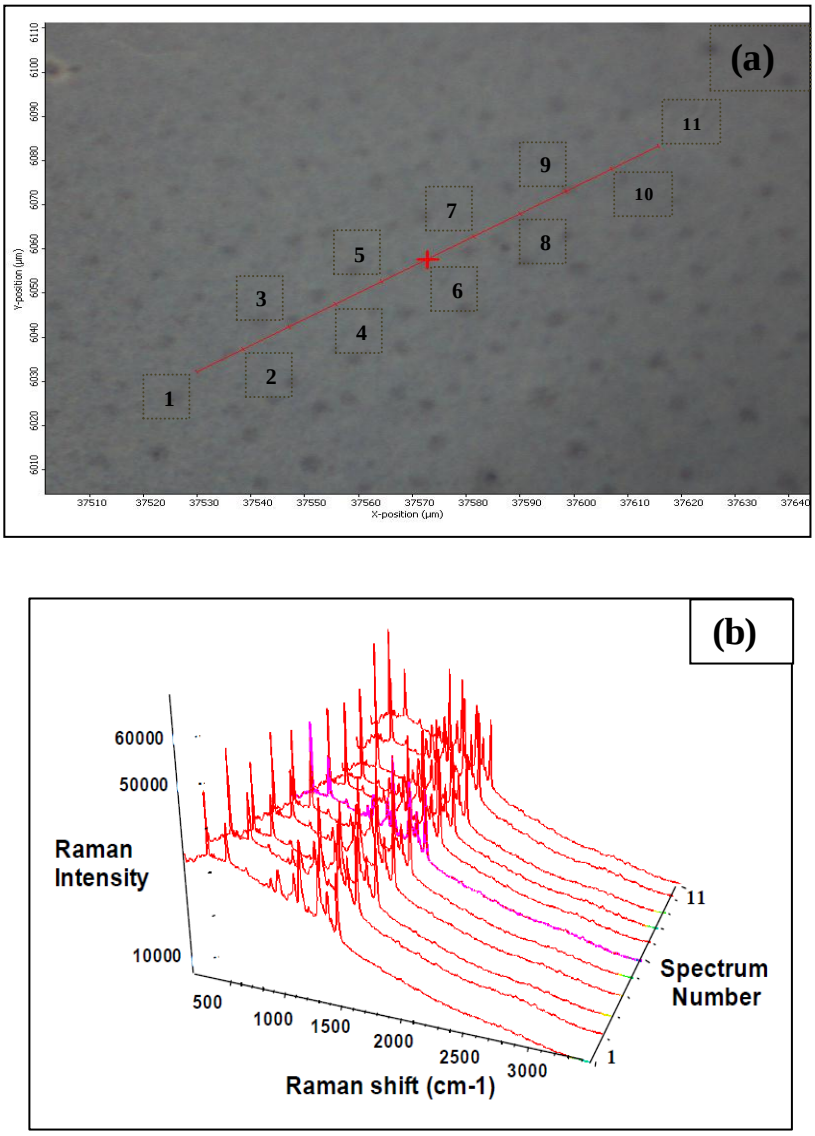

Figure 3.21 The Raman image and Raman spectra of multilayer plasmonic thin films taken at different points a) Bright field image of a multilayer plasmonic film surface. The red line shows the points at where Raman spectra were recorded. b) SERS spectra of R6G recorded at different points shown in (a).

Fig. 3.21 shows the uniformity and repeatability test results for the patterned $Ag/SiO_2/Ag$ multilayer thin films. The SERS measurements were taken from eleven different points shown in Fig. 3.21 (a). It was found that SERS spectra that were taken these points show identical intensities and shapes, indicating that the multilayer thin films provide uniform signal enhancement over the entire substrate surface because of homogeneous structure. The standard deviation of the enhancement factors at 1645 cm^{-1} was calculated to be around 10 % [67].

3.5.1 Enhancement Factor Calculation

In general, the enhancement factor (EF) for Rhodamine 6G (R6G) molecules is calculated by using given formula [68, 69]:

$$EF = (I_{SERS} \,/\, I_{bulk}) \times (N_{bulk} \,/\, N_{surface}) \tag{3.8}$$

In this formula; I_{SERS} represents the vibration intensity in the SERS spectrum of R6G molecule and I_{bulk} represent the vibration intensity in Raman spectra of R6G molecule. N_{bulk} represents the number of molecules under laser light for the bulk sample, and $N_{surface}$ represents the number of molecules in the self-assembled monolayer (SAMs), The $N_{surface}$ and N_{bulk} values can be calculated on the basis of the prediction of the concentration of kinds of surface or bulk sample and the corresponding sampling areas. It is reported that the average surface density of R6G molecules in intensive packed monolayer is approximately one R6G molecule per $4nm^2$ [70]. We used this approximation and assumed the average surface density of R6G monolayer is 4 nm^2. Then the surface coverage area of R6G monolayer on $Ag/SiO_2/Ag$ multilayer thin films was calculated as $4.15x10^{-11}$ $molcm^{-2}$.

$$\Gamma = \frac{1}{(4x10^{-14})x(6.02x10^{23})} = 4.15x10^{-11}\ molcm^{-2} \tag{3.9}$$

$$N_{surface} = \Gamma\, \pi\, {r_{laser}}^2 = (4.15x10^{-11}\ molcm^{-2})\, \pi\, (0.09\ \mu m^2) \tag{3.10}$$

Taking the sampling area (about 0.6 μm in diameter) into account value, $N_{surface}$ has a value of $3.735x10^{-20}$ mol.

For the high numerical apertures of the Raman microscope, depth of field is determined initially through wave optics, while at lower numerical apertures; the

geometrical optical circle of complexity dominates the phenomenon. Using diverse of different conditions for determining when the image becomes inadmissible sharp, a number of authors have proposed different formulas to define the depth of field in a microscope. For the solid sample, the sampling volume is the product of the area of the laser spot (about 0.6μm diameter) and the total depth of field is given by the sum of the wave and geometrical optical depths of fields as the following [71], the penetration depth (~ 1.319 μm) of the focused laser beam.

$$d_{total} = \frac{\lambda_0 n}{NA^2} + \frac{n}{M.NA} e = \frac{532nm}{(0.75)^2} + \frac{14\mu m}{(50)(0.75)} = 1.319\ \mu m \quad (3.11)$$

Where d_{total} represents the depth of field, λ is the wavelength of illuminating light, n represents the refractive index of the medium (air 1.000 or immersion oil 1.515) between the cover slip and the objective front lens element and NA is equal to the objective numerical aperture. The variable *e* is the smallest distance that can be resolved through a detector which is placed in the image plane of the microscope objective, whose lateral magnification is M.

$$N_{bulk} = \frac{d_{total}\ \rho\ \pi\ r_{laser}^2}{M_{weight}} = \frac{(1.319\mu m)(0.79 g cm^{-3})\ \pi\ (0.09\mu m^2)}{479.01 g\ mol^{-1}} \quad (3.12)$$

The density of bulk R6G is nearly equal to 0.79 g cm^{-3} and N_{bulk} can be calculated to be $6.15x10^{-16}$ mol. For 120 nm thickness of SiO_2 layer at 20 ^{0}C at the peak value of 1505 cm^{-1}, the ratio of $I_{surface}$ and I_{bulk} intensities are 34.58. Thus, the enhancement factor was calculated to $5.69x10^5$ [72].

$$EF = (16287/\ 471)\ (6.15x10^{-16}\ /\ 3.735x10^{-20}) = 5.69x10^5 \quad (3.13)$$

The SERS spectra of R6G adsorbed on different SERS substrates were shown in Fig. 3.14. The other calculations were done with this process for the 20 nm, 40 nm, 60 nm and 120 nm at 20 ^{0}C and 450 ^{0}C in Table 3.5.

Table 3.5 Enhancement factor of different SiO_2 thickness of 1505 cm^{-1} Raman shift.

SiO_2 Thickness (nm)	**Enhancement Factor**	
	20 ^{0}C	**450 ^{0}C**
0	$1.48x10^5$	3.83×10^6
20	8.40×10^4	3.40×10^6
40	1.45×10^5	3.77×10^6
60	1.89×10^5	5.01×10^6
120	5.69×10^5	8.41×10^6

The enhancement factor of 10^{-7} M R6G on the annealed multilayer plasmonic SERS substrates was observed as bigger than the enhancement factor of the enhancement factor of 10^{-7} M R6G on the multilayer plasmonic SERS substrates. The enhancement factor of the 10^{-7} M R6G molecules on the $Ag/SiO_2/Ag$ multilayer plasmonic substrates that have different SiO_2 thicknesses at 20 ^{0}C and 450 ^{0}C were increased when the temperature was increased. The enhancement factor of 10^{-7} M R6G on the multilayer plasmonic SERS substrates annealed at 450 ^{0}C was bigger about 25 times than the enhancement factor of 10^{-7} M R6G on the multilayer plasmonic SERS substrates at 20 ^{0}C. The Raman intensities of 10^{-7} M R6G on the multilayer plasmonic SERS substrates for different SiO_2 thicknesses were shown in the Fig. 3.22.

The enhancement factor of 10^{-7} M R6G molecules on the multilayer plasmonic substrates was different for the different peak values. The relationship between enhancement factor and the thickness of SiO_2 was shown in Fig. 3.23.

It was observed that the SiO_2 layer greatly affected the Raman intensity. The SERS EF of the $Ag/SiO_2/Ag$ thin films increased 4-20 folds compared to the single Ag film. The highest enhancement factor was found to be 5.69×10^5 for the multilayer film with 120 nm SiO_2 gap. After annealing, the SERS EF of the $Ag/SiO_2/Ag$ multilayer films increased about 25 times. The Ag/SiO2/Ag multilayer substrate has Ag–air and Ag–SiO_2 interfaces, thus the excited surface plasmons from the Ag surface can be transferred to the top Ag surface through the dielectric SiO_2 spacers. Hence, the conduction electrons on the silver surface were further localized. As a result, the SiO_2 interlayer plays an important role in enhancing the Raman signals for multilayer films

[13]. Lian C. T. Shoute prepared Ag/SiO_2/AgIF SERS active multilayer films and suggested that optical interference effect was the predominant contributor to the SPR absorption by multilayer substrates. Coupling between LSPR and Surface plasmon polaritons (SPPs) were negligible at larger dielectric layers [22].

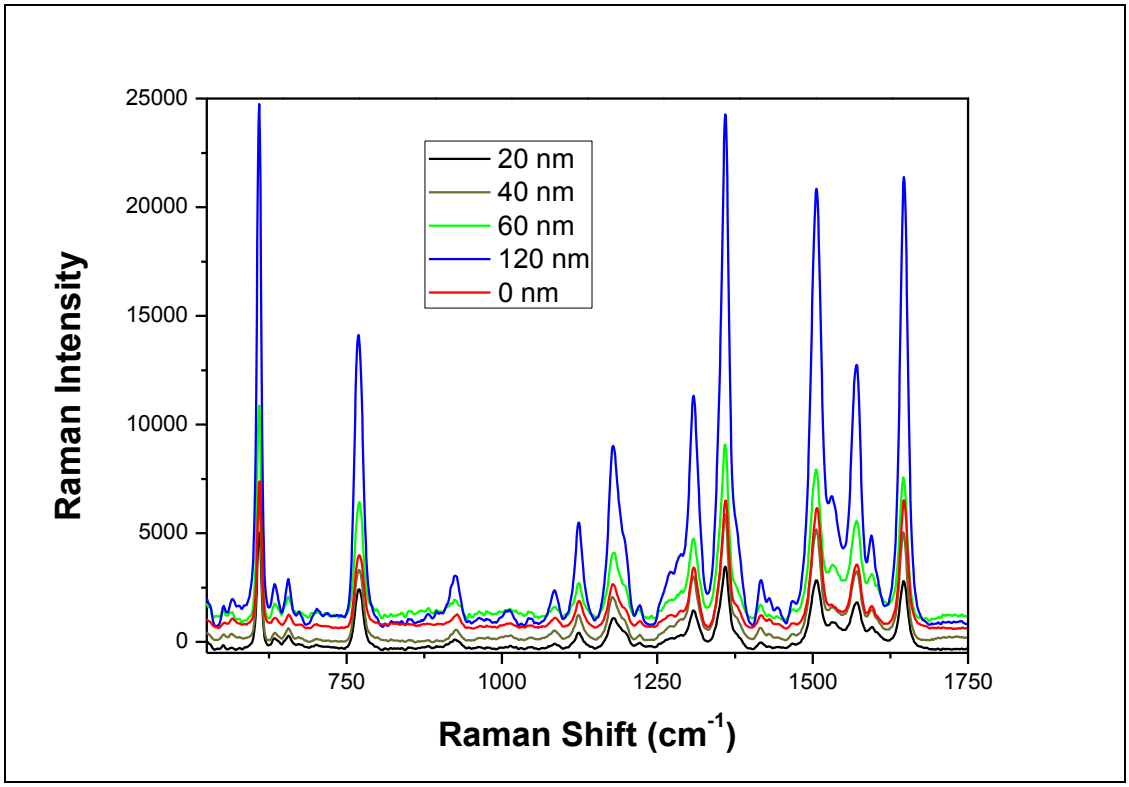

Figure 3.22 SERS spectra of R6G molecules on the multilayer plasmonic surface.

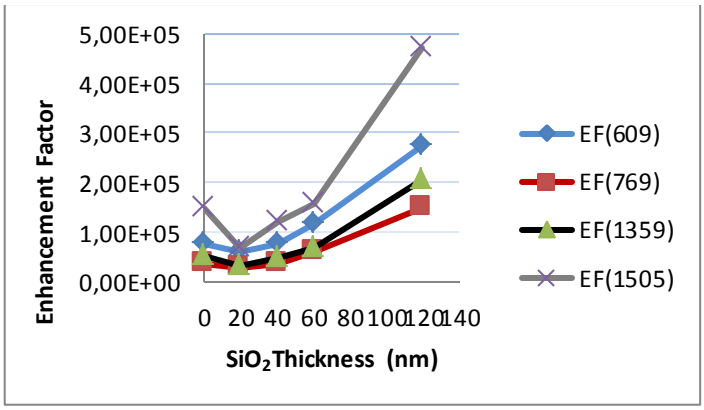

Figure 3.23 Enhancement Factor versus Thicknesses of SiO_2 at 20 ^{0}C for different strong peaks of R6G.

CHAPTER 4

CONCLUSION

The $Ag/SiO_2/Ag$ multilayer thin films were deposited in sequence on glass by E-Beam Evaporation. After deposition, sample films with different thicknesses of SiO_2 layer (20 nm, 40 nm, 60 nm and 120 nm) were annealed at 450 °C. This annealing resulted in different enhancement factor of Ag nanoparticles on SiO_2 surface. The SERS results confirmed that thicker deposited Ag layer resulted in larger Ag enhancement factor with enhancement factor from 8.40×10^4 to 8.41×10^6.

For the optical analysis, the optical absorbance of Ag nanoparticles on SiO_2 was experimentally investigated. With the increased enhancement factor of Ag films, the surface plasmon resonance was enhanced along the metal/dielectric/metal interface, leading to a broader optical absorption as observed by UV–Vis spectrophotometer.

For the surface analysis, the surface roughness of $Ag/SiO_2/Ag$ multilayer thin films was determined using AFM and the dependency of roughness value on increasing total thickness of multilayer thin films was investigated. The surface topography of Ag nanoparticles was examined by using SEM image. The crystallite size of deposited Ag nanoparticles on SiO_2 was determined by using two different calculation methods such as Scherrer and Williamson- Hall methods at 20 °C and annealed at 450 °C. The basis of these methods is to calculate the FWHM (Full Width at Half Maximum) of strong peak (111) of XRD pattern. The crystallite size of Ag nanoparticles increased with increasing temperature. Also, strain, stress and energy density values were determined. These values were decreased with increasing temperature.

This thesis study showed that the existence of SiO_2 layer between Ag metal films leaded to higher scattering intensity and more regions of strong field enhancement

compared to single layer Ag film. The fabricated $Ag/SiO_2/Ag$ thin films hold a great potential in the applications of surface-enhanced Raman scattering and in the development of SERS active substrates.

REFERENCES

[1] Lin, W.C., Yang, M.C., "Novel silver/poly (vinyl alcohol) nanocomposites for surface-enhanced Raman scattering-active substrates", *Macromol Rapid Commun*, Vol. 26, pp. 1942-1947, 2005.

[2] Badr, Y., Mahmoud, M.A., "Enhancement of the optical properties of poly vinyl alcohol by doping with silver nanoparticles", *Journal of Applied Polymer Science*, Vol. 99, pp. 3608, 2006.

[3] Hong, KH, Park, JL, Sul, IH, Youk, JH, Kang, TJ, "Preparation of antimicrobial poly(vinyl alcohol) nanofibers containing silver nanoparticles", *Journal of Polymer Science: Part B: Polymer Physics*, Vol. 44, pp. 2468, 2006.

[4] Beecroft, L.B., Ober, C.K., "Nanocomposite materials for optical applications", *Chemistry of Materials*, Vol. 9, pp. 1302, 1997.

[5] Mbhele, Z.H., Salemane, M.G., Van Sittert, C.G.C.E., Nedeljkovi´c, J.M., Djokovi´c, V., and Luyt, A.S., "Fabrication and Characterization of Silver-Polyvinyl Alcohol Nanocomposites", *Chemistry of Materials,* Vol. 15, pp. 5019, 2003.

[6] Brolo, A.G., Arctander, E., Gordon, R., Leathem, B. and Kavanagh, K.L., "Nanohole enhanced Raman scattering", *Nano Letters*, Vol. 4, pp. 2015–2018, 2004.

[7] Zhang, X., Zhao, J., Whitney, A., Elam, J. and Van Duyne, R.P., "Ultrastable Substrates for Surface Enhanced Raman Spectroscopy Fabricated by Atomic Layer Deposition: Improved Anthrax Biomarker Detection", *Journal of the American Chemical Society*, Vol. 128, pp. 10304-10309, 2006.

[8] Zhang, BH, Wang, HS, Lu, LH, Ai, KL, Zhang, G, Cheng, XL, "Large-area silvercoated silicon nanowire arrays for molecular sensing using surface enhanced Raman spectroscopy", *Advanced Functional Materials*, Vol. 18, pp. 2348–2355, 2008.

[9] Hasell, T., Lagonigro, L., Peacock, A.C. , Yoda, S., Brown, P.D., Sazio, P.J.A., Howdle, S.M., *Advance Functional Materials*, Vol. 18, pp. 1265-1271, 2008.

[10] Budak, S., Guner, S., Minamisawa, R.A., ILA, D., "MeV Si ions bombardment effects on the thermoelectric properties of nano-layers of nanoclusters of Ag in SiO2 host", *Surface and Coatings Technology*, Vol. 203, pp. 2479-2481, 2009.

[11] Kelly, K. L., Coronado, E., Zhao, L. L., Schatz, G. C., "The optical properties of metal nanoparticles: The influence of size, shape, and dielectric environment", *Journal of Physical Chemistry B*, Vol. 107, pp. 668–677, 2003.

[12] Wu, D. Y., Li, J. F., Ren, B., Tian, Z. Q., "Electrochemical surface-enhanced Raman spectroscopy of nanostructures", *Chemical Society Review*. Vol. 37, pp. 1025–1041, 2008.

[13] Kyoung, H.K., Youn-Kyoung, B., Hwan-Jin, J., Mohan, S. Hee-Tae, J., "Cylindrical posts of Ag/SiO_2/Au multi-segment layer patterns for highly efficient surface enhanced Raman scattering", *Nanotechnology*, Vol. 23, pp. 315302, 2012.

[14] Arenas, J. F., Castro, J. L., Otero, J. C., Marcos, J. I., "Study of interaction between aspartic acid and silver by surface-enhanced Raman scattering on H_2O and D_2O sols", *Biopolymers*, Vol. 62, pp. 241-248, 2001.

[15] Castro, J. L., Montanez, M. A., Otero, J. C., Marcos, J. I., "SERS and Vibrational Spectra of Aspartic Acid", *Journal of Molecular Structure*, Vol. 349, pp. 113-116, 1995.

[16] Vanduyne, R. P., Hulteen, J. C., Treichel, D. A., "Atomic-Force Microscopy and Surface-Enhanced Raman-Spectroscopy .1. Ag Island Films and Ag Film over Polymer Nanosphere Surfaces supported on Glass", *Journal of Chemical Physics*, Vol. 99, pp. 2101-2115, 1993.

[17] Suh, J. S., Moskovits, M., "Surface-Enhanced Raman Spectroscopy of Amino Acids and Nucleotide Bases Adsorbed on Silver", *Journal of the American Chemical Society*, Vol. 108, pp. 4711-4718, 1986.

[18] Podstawka, E., Ozaki, Y., Proniewicz, L. M., "Part III: Surface-enhanced Raman scattering of amino acids and their homodipeptide monolayers deposited onto colloidal gold surface", *Applied Spectroscopy* Vol. 59, pp. 1516-1526, 2005.

[19] Podstawka, E., Ozaki, Y., Proniewicz, L. M., "Part II: Surface-enhanced Raman spectroscopy investigation of methionine containing fleterodipeptides adsorbed on colloidal silver", *Applied Spectroscopy*, Vol. 58, pp. 581-590, 2004.

[20] Castro, J. L., SanchezCortes, S., Ramos, J. V. G., Otero, J. C., Marcos, J. I., "Surface-enhanced Raman spectroscopy of gamma-aminobutyric acid on silver colloid surfaces", *Biospectroscopy*, Vol. 3, pp. 449-455, 1997.

[21] Ooka, A. A., Kuhar, K. A., Cho, N. J., Garrell, R. L., "Surface interactions of a homologous series of alpha,omega-amino acids on colloidal silver and gold", *Biospectroscopy*, , Vol. 5, pp. 9-17, 1999.

[22] Lian, C. T. Shoute "Multilayer Substrate-Mediated Tuning Resonance of Plasmon and SERS EF of Nanostructured Silver", *ChemPhysChem*, Vol. 11, pp. 2539-2545, 2010.

[23] Min, Q., Pang, Y., Collins, D.J., Kuklev, N.A., Gottselig, K., Steuerman, D.W., Gordon, R., "Substrate-based platform for boosting the surface-enhanced Raman of plasmonic nanoparticles", *Optics Express*, Vol. 19, pp. 1648-55, 2011.

[24] Büyükbakkal, Ö., *Optical and Conducting Properties of Co Doped ZnO Thin Films*, M.S. Thesis, Fatih University, 2012.

[25] Schematic diagram of e-beam evaporation system, http://www.ece.utep.edu/research/webedl/cdte/Fabrication/index.htm

[26] Harvey, D., *Modern Analytical Chemistry*, McGraw Hill, 2000.

[27] Mortimer, C.E., *Modern Üniversite Kimyası*, Çağlayan Bookstore, İstanbul, 1999.

[28] Skoog, D.A., West, D.M., Holler, F.J., *Fundamentals of Analytical Chemistry*, Saunders College Publishing, Seventh Edition.

[29] Yıldız, A., Genc, O., Bektas, S., *Enstrumental Analiz Yontemleri*, Hacettepe University Publications, 1997.

[30] Surface plasmon, http://en.wikipedia.org/wiki/Surface_plasmon.

[31] Raman, C.V. and Krishnan, K.S., "A New Type of Secondary Radiation", *Nature*, Vol. 121, pp. 501-502, 1928.

[32] Kaur, H.S., *Instrumental Methods of Chemical Analysis, third edition*, Pragati Prakashan, Meerut, 2006.

[33] Molecular energy diagram of Rayleigh and Raman scattering, http://cnx.org/content/m34528/latest/#id1168942932554.

[34] Bugay, D.E., Martogolio Smith, P.A. Jickells, S., Negrusz, A., (Eds.) Clarke's Analytical Forensic Toxicology, third edition, Pharmaceutical Press, London, 2008.

[35] Fleischmann, M., Hendra, P.J. and McQuillan, A.J., "Raman spectra of pyridine adsorbed at a silver electrode", *Chemical Physics Letters*, Vol. 26, pp. 163-166, 1974.

[36] Graham, D. and Goodacre, R., "Chemical and bioanalytical applications of surface enhanced Raman scattering spectroscopy" *Chemical Society Review*, Vol. 37, pp. 883-884, 2008.

[37] Volkan, M., Stokes, D.L. and Vo-Dinh, T., "Surface-enhanced Raman of dopamine and neurotransmitters using sol-gel substrates and polymer-coated ber-optic probes," *Applied Spectroscopy*, Vol. 54, pp. 1842-1848, 2000.

[38] Lesueur, A., Kumar, L.K.S., Gordon, R.,"Apex-enhanced second-harmonic generation by using double-hole arrays in a gold", *Physics Review B*, Vol. 75, pp. 45423, 2007.

[39] Aslan, K., Gryczynski, I., Malicka, J., Matveeva, E., Lakowicz, J.R. and Geddes, C.D., "Metal-enhanced fluorescence: An emerging tool in biotechnology", *Current Opinion Biotechnology*, Vol. 16, pp. 55-65, 2005.

[40] Coe, J.V., Heer, J.M., Teeters-Kennedy, S., Tian, H. and Rodriguez, K.R., "Extraordinary transmission of metal l ms with arrays of subwavelength holes", *Annual Review Physics Chemical*, Vol. 59, pp. 179-202, 2008.

[41] Bordenyuk, A.N., Weeraman, C., Yatawara, A., Jayathilake, H.D., Stiopkin, I., Yi, L. and Benderskii, A.V., "Vibrational sum frequency generation spectroscopy of dodecanethiol on metal nanoparticles", *Journal Physics Chemical*, Vol. 111, pp. 8925-8933, 2007.

[42] Blackie, Evan J.; Le Ru, Eric C.; Etchegoin, Pablo G., "Single-Molecule Surface-Enhanced Raman Spectroscopy of Nonresonant Molecules", *Journal American Chemical Society*, Vol. 131, pp. 14466-14472, 2009.

[43] Plasmon oscillations for small metallic sphere, http://nanocomposix.com/technology/plasmonics-and-nanophotonics.

[44] Nie, S; Emory, SR, "Probing Single Molecules and Single Nanoparticles by Surface-Enhanced Raman Scattering", *Science*, Vol. 275, pp. 1102-6, 1997.

[45] Kelly, K. L., Coronado, E., Zhao, L. L. and Schatz, G. C., "The optical properties of metal nanoparticles: The infuence of size, shape, and dielectric environment", *Journal of Physical Chemical B*, Vol. 107, pp. 668-677, 2003.

[46] Richard, J. C. B., Jian, W., Ratna T., Rachel E. Y., Martin J. T. M., "Electromagnetic modelling of Raman enhancement from nanoscale substrates: a route to estimation of the magnitude of the chemical enhancement mechanism in SERS", *Faraday Discussions*, Vol. 132, pp. 201-203, 2006.

[47] Hao, E. and Schatz, G. C., "Electromagnetic elds around silver nanoparticles and dimers," *Journal of Chemical Physics*, Vol. 120, pp. 357-366, 2004.

[48] Wu, D.Y., Li, J.F., Ren, B. and Tian, Z.Q., "Electrochemical surface-enhanced Raman spectroscopy of nanostructures", *Chemical Society Review*, Vol. 37, pp. 1025-1041, 2008.

[49] Moskovits, M., "Surface-enhanced spectroscopy", *Reviews of Modern Physics*, Vol. 57, pp. 783-826, 1985.

[50] Otto, A., "The 'adatom model' of SERS, the present status", *Surface Science*, Vol. 138, pp. 319-338, 1984.

[51] Aslan, A., Gölcük, K., Bozkurt, A., "Nanocomposite polymer electrolytes membranes based on Poly (vinylphosphonic acid)/SiO_2", *Journal of Polymer Research*, Vol. 19, pp. 1-8, 2012.

[52] Sedin, D.L., Rowlen, K.L., "Influence of tip size on AFM roughness measurements", *Applied Surface Science*, Vol.182, pp. 40–48, 2001.

[53] Wang, L., Zhang, Y., Zeng, G., Xi S., "Preparation of TiO_2 film through hydrolysis of titanium butoxide and interaction between sensitizing dyes and the film", *Acta Physico-Chimica Sinica* , Vol. 13, pp. 753-757, 1997.

[54] B.D. Cullity, Elements of X-ray Diffraction, Addison-Wesley Company, USA.

[55] Rita, J., Sasi, F., "Structural and Optical properties of ZnS nanoparticles synthesized by solid state reaction method", *Chalcogenide Letters*, Vol. 6, pp. 535, 2009.

[56] Theivasanthi, T. and Alagar, M., "X-Ray Diffraction Studies of Copper Nanopowder", *Archives of Physics Research*, Vol. 1, pp. 112, 2010.

[57] Birkholz, M., "Thin Film Analysis by X-ray Scattering", Wiley-VCH Verlag GmbH and Co. KGaA, Weinheim, 2006.

[58] Khan, M.A.M., Kumar, S., Ahamed M., Alrokayan S.A., AlSalhi M.S., "Structural and thermal studies of silver nanoparticles and electrical transport study of their thin films", *Nanoscale Research Letter*, Vol. 6, pp. 434, 2011.

[59] Hildebrandt, P., Stockburger, M., "Surface-Enhanced Resonance Raman-Spectroscopy of Rhodamine-6G Adsorbed On Colloidal Silver", *Journal of Physical Chemistry*, Vol. 88, pp. 5935-5944, 1984.

[60] Michaels, A. M., Nirmal, M., Brus, L. E., "Surface enhanced Raman spectroscopy of individual rhodamine 6G molecules on large Ag nanocrystals", *Journal of the American Chemical Society*, Vol. 121, pp. 9932-9939, 1999.

[61] Michaels, A. M., Jiang, J., Brus, L., "Ag nanocrystal junctions as the site for surface-enhanced Raman scattering of single Rhodamine 6G molecules", *Journal of Physical Chemistry B*, Vol. 104, pp. 11965-11971, 2000.

[62] Tian, Z. Q., Ren, B., Wu, D. Y., "Surface-enhanced Raman scattering: From noble to transition metals and from rough surfaces to ordered nanostructures", *Journal of Physical Chemistry B*, Vol. 106, pp. 9463-9483, 2002.

[63] Güvenç, H. O., *Surface Enhanced Raman Scattering From Au and Ag Nanoparticle Coated Magnetic Microspheres*, M.S. Thesis, Bilkent University, 2008.

[64] Wang, T., Turhan, M., Gunasekaran, S., "Selected properties of pH-sensitive, biodegradable chitosan–poly(vinyl alcohol) hydrogel", *Polymer International*, Vol. 53, pp. 911, 2004.

[65] Liu, Y. C., Lin, P.I., Chen, Y.T., Ger, M. D., Lan, K. L., Lin, C. L., “"Effect of TiO2 Nanoparticles on the Improved Surface-Enhanced Raman Scattering of Polypyrrole Deposited on Roughened Gold Substrates”, *The Journal of Physical Chemistry B*, Vol. 108, pp. 14897–14900, 2004.

[66] Sajjadi, S., Brooks, B.W., “Unseeded semibatch emulsion polymerization of butyl acrylate: Bimodal particle size distribution”, *Journal of Polymer Science, Part A: Polymer Chemistry*, Vol. 38, pp. 528, 2000.

[67] Kyoung, H. K., Youn-Kyoung, B., Hwan-Jin, J., Mohan, S., Hee-Tae, J., “Cylindrical posts of Ag/SiO_2/Au multi-segment layer patterns for highly efficient surface enhanced Raman scattering”, *Nanotechnology*, Vol. 23, pp. 315302, 2012.

[68] Cai, W.B., Ren, B., Li X.Q., She, C.X., Liu, F.M., Cai, X.W.,Tian, Z.Q., “Investigation of Surface-Enhanced Raman Scattering from Platinum Electrodes Using A Confocal Raman Microscope: Dependence of Surface Roughening Pretreatment”, *Surface Science*, Vol. 406, pp. 9-22, 1998.

[69] Yu, H.Z., Zhang, J., Zhang, H.L., Liu, Z.F., “Surface-enhanced Raman scattering (SERS) from azobenzene self-assembled "sandwiches"”, *Langmuir*, Vol. 15, pp. 16-19, 1999.

[70] Kudelski, A., “Raman studies of Rhodamine 6G and crystal violet sub-monolayers on electrochemically roughened silver substrates: Do dye molecules adsorb preferentially on highly SERS-active sites”, *Chemical Physics Letters*, Vol. 414, pp. 271-275, 2005.

[71] Depth of Field Calculator, http://www.microscopyu.com/tutorials/java/depthoffield/index.html

[72] Dan, L., Da-Wei, L., Yang, L., John, S.F., Yi-Tao, L., “Cyclic Electroplating and Stripping of Silver on Au/SiO2 core/shell Nanoparticles for Sensitive and Recyclable Substrates of Surface-enhanced Raman Scattering” Supplementary Material (ESI) for Journal of Materials Chemistry This journal is The Royal Society of Chemistry 2010.